Q. J. R. Meteorol. Soc. (1997), **123**, pp. 953–981

The singular vectors of a coupled ocean–atmosphere model of ENSO. I: Thermodynamics, energetics and error growth

By A. M. MOORE*[1] and R. KLEEMAN[2]
[1]*University of Colorado at Boulder, USA*
[2]*Bureau of Meteorology Research Centre, Australia*

(Received 23 November 1995; revised 26 June 1996)

SUMMARY

The singular vectors of a dynamical system are the most rapidly growing perturbations that can exist in the system before nonlinearity becomes important. We have studied the singular vectors of an intermediate coupled ocean–atmosphere model of El Niño/Southern Oscillation (ENSO) in an effort to understand the dynamics responsible for the growth of small perturbations in the tropics. In particular, we have examined how the singular vectors of the observed seasonal cycle are influenced by various thermodynamic processes which operate in the upper-ocean mixed-layer, and which affect sea-surface temperature (SST). These processes include vertical movements of the main thermocline, zonal advection and vertical upwelling. The main findings are:

- the singular vector spectrum is dominated by the fastest growing member, regardless of which thermodynamic processes are active;
- the growth factors of the singular vectors exhibit a strong seasonal dependence;
- the western and central parts of the Pacific Ocean are the areas most often favoured for growth by the singular vectors, and the general criteria that must be met for singular-vector growth have been determined;
- at a given time of year, the growth factors of the singular vectors are sensitive to different combinations of thermodynamic processes, although the configuration of the dominant singular-vector wind field after optimal growth has been achieved is very similar in all cases. This suggests that in the tropics, the coupled system has a preferred response that the ocean thermodynamics controlling SST conspire to produce, regardless of which processes are operating in the mixed layer;
- the observed ENSO cycle is likely to influence singular-vector growth significantly.

These results and ideas have important ramifications for the growth of errors and uncertainties in models during ENSO forecasts, and for the way this influences the predictability of ENSO. They also have important ramifications for the way perturbations grow in the real coupled ocean–atmosphere system.

KEYWORDS: Atmosphere–ocean interaction Oceanic mixed layer Predictability Seasonal forecasts Sea-surface temperature Singular vectors Tropical meteorology

1. INTRODUCTION

For almost a decade, forecasts of El Niño/Southern Oscillation (ENSO) have been made using a variety of numerical models and statistical techniques. (See Latif *et al.* (1994), Barnett *et al.* (1994) and Barnston *et al.* (1994) for excellent reviews.) Most of the forecast models and techniques developed show significant skill, and reliable predictions can be made up to 12 months in advance. However, while some forecasts of ENSO are very successful, others fail utterly. There is also evidence that the predictability of ENSO varies seasonally (Zebiak and Cane 1987; Goswami and Shukla 1991; Latif and Graham 1991; Latif *et al.* 1993), and that it also depends on techniques of data assimilation and initialization (Kleeman *et al.* 1995; Chen *et al.* 1997; Rosati *et al.* 1997). In addition, despite their complexity, state-of-the-art coupled ocean–atmosphere general-circulation models (GCMs) do not show a greater skill than much simpler models. Clearly then, if we are to improve the forecasting capabilties of our models and their reliability, we must develop an understanding of the processes that influence the growth of forecast errors and limit the predictability of dynamic systems.

* Corresponding author: Program in Atmospheric and Oceanic Sciences, University of Colorado at Boulder, Campus Box 311, Boulder, CO 80309, USA.

Probably the most important factor that will influence the predictability of ENSO is the rate at which errors and uncertainties in the initial conditions for the model will grow with time. This in turn will depend on the stability of dynamical flows in the system at the time that a forecast is made.

Attempts have been made to understand the dynamics of error growth in models of ENSO, using new and emerging ideas about the linear growth of instabilities in systems described by non-normal dynamical operators (Blumenthal 1991; Palmer *et al.* 1994; Xue *et al.* 1994; Penland and Sardeshmukh 1995; Moore and Kleeman 1996; Chen *et al.* 1997; Kleeman and Moore 1997; Xue *et al.* 1997). Some of these ideas can be attributed to the early work of Lorenz (1965) who first argued that the early stages of forecast-error growth in numerical weather-prediction models can be understood in terms of the growth of the singular vectors of the forecast-error norm. Recently there has been a resurgence of these ideas in numerical weather-prediction (Farrell 1990; Palmer 1993), and singular-vector techniques are now used operationally at the European Centre for Medium-Range Weather Forecasts (ECMWF) (Buizza *et al.* 1993; Mureau *et al.* 1993; Buizza and Palmer 1995). Similar ideas have been applied by Farrell (1982, 1985, 1988) to explain mid-latitude cyclogenesis in the atmosphere, and by Farrell and Moore (1992) and Moore and Farrell (1993, 1994) to understand the dynamics of instabilities in the ocean.

The work described in the present paper is an extension of recent studies by Moore and Kleeman (1996), hereafter MK96, and Kleeman and Moore (1997), in which singular-vector techniques were used to examine the growth of errors in an intermediate coupled ocean–atmosphere model, and the relationship of this growth to the predictability of ENSO. MK96 found that areas where conditions were most favourable for the rapid amplification of errors were in western and central parts of the tropical Pacific Ocean. Their study, however, was restricted to a system in which only vertical movements of the oceanic thermocline were allowed to influence errors in the sea-surface temperature (SST) directly, since earlier work by Kleeman (1993) revealed that this thermodynamic mechanism alone can explain much of the skill associated with ENSO forecasts. It is envisaged by many that, ultimately, coupled ocean–atmosphere GCMs will form the backbone of ENSO prediction systems. Such models include a full range of upper-ocean thermodynamic processes which can influence SST, and studies of tropical interannual variability in coupled GCMs reminiscent of the observed ENSO signal have shown the models to be simulating dynamically very complex systems. Building on MK96, we have examined the influence of upper ocean thermodynamics on the structure and growth of the singular vectors of an intermediate coupled model. The present work is important because it shows how different thermodynamic processes can combine to produce error growth, information that will also be valuable for interpreting coupled-GCM predictions of ENSO. In addition, we demonstrate the role played by the seasonal cycle in enhancing error growth in certain geographical areas at different times of year.

In Part II of this study, (Moore and Kleeman 1997), we examine some basic sensitivities of the coupled-model singular-vectors to a number of parameters that define them. We also examine the dynamical significance of the singular vectors and how they relate to the ENSO cycle.

The present paper is laid out in the following way. In section 2 we present a brief description of the coupled-model used. The tools and procedures used for computing the coupled-model singular-vectors are described in section 3. In section 4 we explore the influence of upper-ocean thermodynamics on the structure and growth of the singular vectors of the coupled system. A discussion of the likely influence of the observed ENSO cycle on perturbation growth and predictability, and a discussion of all our findings, can be found in sections 5 and 6 respectively.

2. THE COUPLED MODEL

The coupled model that we have used in this study is the intermediate coupled model of Kleeman (1993), hereafter K93, which is currently used operationally at the Australian Bureau of Meteorology Research Centre as part of their seasonal outlook and forecasting system. The model is described in detail by K93 so only a brief description of it will be given here.

(*a*) *The atmospheric model*

The atmospheric component of the coupled model is a linear, two-pressure-level model on a β-plane, as described in detail by Kleeman (1989, 1991). Following Gill (1980), it is a steady-state dynamical model, being global in extent, with a horizontal resolution of approximately 2.8°. The model pressure-levels are centred at 250 mb and 750 mb, and the model equations of motion are linearized about a state of rest. Dissipation is included in the form of Rayleigh friction and Newtonian damping terms. In addition, a direct thermal-forcing term relaxes the 750 mb geopotential-height anomaly to the surface-temperature anomaly, a formulation which has been widely used in the literature to mimic the effects of surface processes associated with radiation, sensible-heat fluxes and shallow convection which are not explicitly modelled (e.g. Gill 1985; Davey and Gill 1987).

It has been known for some time that heating anomalies associated with deep penetrative convection in the atmosphere are important during the onset of ENSO events in the western parts of the tropical Pacific Ocean. With this in mind, the atmospheric model is also forced by a mid-tropospheric-heating anomaly Q which represents latent-heating anomalies arising from anomalous deep penetrative convection, namely:

$$Q = \frac{L_v \rho_4 c_E}{c_p \rho_2 I_1}\left[|\mathbf{U}|\{q_{\text{diff}}(\overline{T}+T')\} + |\overline{\mathbf{U}}|\{q_{\text{diff}}(\overline{T}+T') - q_{\text{diff}}(\overline{T})\}\right]$$
$$+\frac{L_v I_2}{c_p \rho_2 I_1}\left\{(\overline{q}+q)\nabla\cdot\mathbf{U} + q\nabla\cdot\overline{\mathbf{U}} + (\overline{\mathbf{U}}+\mathbf{U})\cdot\nabla q + \mathbf{U}\cdot\nabla\overline{q}\right\}. \qquad (1)$$

This expression results from integrating the atmospheric-moisture equation vertically, where I_1 and I_2 are constants of integration. In (1), L_v is the latent heat of evaporation, c_E is the latent-heat exchange-coefficient, c_p is the the specific heat capacity at constant pressure, and ρ_4/ρ_2 is the ratio of the air density at 1000 mb to that at 500 mb. An overbar denotes the observed mean value, while all other quantities represent anomalies. In (1), $\overline{T}$ and T' are the mean and anomalous SST; $\mathbf{U}$ is the wind velocity; $q_{\text{diff}}(T)$ is the air–sea specific-humidity difference at temperature T; q is the specific humidity, and $\overline{q}$ the specific humidity at temperature $\overline{T}$. All other symbols have their usual meanings. The first term in square brackets represents evaporation anomalies and the second term represents the effects of anomalous moisture-convergence. Penetrative convection in the atmosphere occurs predominantly in areas where SST > 28°C (Hirst 1986). Circulation anomalies can cause SST to fall below this critical value, causing penetrative convection to switch off and so giving rise to heating anomalies $Q = -\overline{Q}$, where $\overline{Q}$ is the mean latent-heating rate computed from observations. This effect is incorporated in the atmospheric model by comparing the moist static energy of air parcels $m(\overline{T}+T')$ with a critical value m_c, below which penetrative convection cannot occur. A full discussion of the form of Q and the condition for penetrative convection is given in Kleeman (1991). The observed seasonal cycle of the coupled ocean–atmosphere system is prescribed in the model through $\overline{T}$, $\overline{\mathbf{U}}$ and $\overline{q}$ in the heating function Q of (1).

The performance of the atmospheric model has been the subject of rigorous examination by Kleeman (1991) and Kleeman *et al.* (1992); in general, the model gives a good depiction of the wind anomalies associated with ENSO SST-anomalies.

(*b*) *The ocean model*

The ocean component of the coupled model solves the wind-forced, linear, shallow-water equations for a single baroclinic mode on an equatorial β-plane, subject to the long-wave approximation (Cane and Sarachik 1981; Gill 1982). Dissipation is included in the form of Rayleigh friction and Newtonian cooling. The model domain is limited to the tropical Pacific Ocean between 115°E and 80°W, 30°S to 30°N, with a grid spacing of approximately 1/2°.

Changes in the zonal and meridional currents, u and v, and the depth of the main thermocline, give rise to changes in the ocean SST. The SST anomalies, T', along the equator are modelled by the equation

$$\frac{\partial T'}{\partial t} = \underbrace{\eta h}_{\text{(i)}} \underbrace{- \{\Delta(\overline{w} + w) - \Delta(\overline{w})\}\frac{\partial \overline{T}}{\partial z}}_{\text{(ii)}} \underbrace{- \overline{u}\frac{\partial T'}{\partial x} - u\frac{\partial(\overline{T} + T')}{\partial x}}_{\text{(iii)}} \underbrace{- \epsilon T' + \kappa\frac{\partial^2 T'}{\partial x^2}}_{\text{(iv)}}. \quad (2)$$

Term (i) in (2) models the influence of thermocline displacements on T' in the presence of mean upwelling. For convenience, we shall refer to term (i) as the 'thermocline term'. The parameter η is the constant of proportionality (or regression coefficient) that relates SST anomalies to thermocline-depth anomalies h. Different values are used for η in the western and eastern Pacific Ocean to reflect the fact that the main thermocline is deeper in the west than the east. As a result, a given latent-heating anomaly is associated with larger SST-anomalies in the east than in the west. In the eastern Pacific, from the coast of Central America to 140°W, $\eta = \eta_E = 3.4 \times 10^{-8}$ °C m^{-1}s^{-1}, while in the western Pacific, $\eta = \eta_W = \eta_E/5$. In the central Pacific, between 140°W and the date line, η_C varies linearly between η_E and η_W. Steady-state solutions of (2) with term (i) and dissipation alone yield $T' = 2$°C when $h = 15$ m. The parameter η can also vary seasonally in accordance with the seasonal cycle in mean upwelling $\overline{w}$. In (2), $|h| \leqslant h_{max}$, where h_{max} is a cut-off value of h which crudely mimics nonlinearities in the real ocean and prevents a runaway instability developing in the coupled system.

Term (ii) in (2) models the influence of anomalous Ekman-induced upwelling at the equator on T'. The velocities w and $\overline{w}$ are, respectively, the anomalous and mean vertical-upwelling velocities at the base of the mixed layer, and are computed by assuming that a shear flow exists between the mixed layer and the deep levels of the ocean. The vertical velocity is then proportional to the divergence of the total current in the mixed layer. Full details of this calculation were given by Zebiak and Cane (1987), Phlips (1987), Neelin (1991) and K93. The Heaviside function Δ allows only upwelling to influence T'; downwelling has no effect on T'. The mean vertical temperature-gradient $\partial\overline{T}/\partial z$ has a constant value, and the sensitivity of the coupled model to choices of $\partial\overline{T}/\partial z$ is discussed in K93.

Term (iii) in (2) models the influence of anomalous zonal advection on SST. The observed mean SST, $\overline{T}$, is computed from the US Climate Analysis Center (CAC) analyses, while the total-mean and perturbation zonal-velocities $\overline{u}$ and u are computed by assuming that a shear flow exists between the mixed layer and deep levels of the ocean as described above. The mean current $\overline{u}$ is computed by running the ocean model alone, forced only by observed, climatological, winds.

Term (iv) in (2) is a combination of a relaxation term (included to model negative feedback effects (Battisti and Hirst 1989; Neelin 1990)), and a weak eddy-diffusivity. A fixed Gaussian structure-function is used in the meridional direction to compute off-equatorial SST-anomalies. The e-folding length-scale of the meridional structure-function is 10° which is close to the atmospheric equatorial radius of deformation. Such a simplification was also made by Neelin (1991) and reflects the assumption that effects such as meridional advection and the differing meridional structure of the horizontal modes, are unimportant to the primary ENSO-mechanism.

Prior to coupling the ocean and atmosphere models, the ocean model is spun-up using the wind-stress anomalies computed from the Florida State University (FSU) wind products (Legler and O'Brien 1984). In coupled mode, the SST anomalies computed from (2) are usually incorporated into the atmospheric model once each month and are superimposed on the monthly CAC SST-climatology, although more frequent coupling is possible and straightforward. The resulting surface wind anomalies computed by the atmospheric model are converted to surface wind stress anomalies using a linear stress law.

As described by K93, the coupled model achieves correlations with the observed NINO3 index in excess of 0.5 for lead times out to 11 months, a level of skill similar to that of the models of Zebiak and Cane (1987) and Latif *et al.* (1993).

3. Computation of singular vectors

The stability of the coupled system to perturbations, resulting from (say) uncertainties in the initial conditions, will depend upon the nature of the dynamical operators describing the system. To understand this, suppose that ψ represents the state vector describing the coupled system which evolves according to

$$\frac{\partial \psi}{\partial t} = L(\psi), \tag{3}$$

where $L(\psi)$ is a nonlinear operator. During their early stages of linear development, small perturbations $\delta\psi$ to ψ will evolve according to

$$\frac{\partial \delta\psi}{\partial t} = \left(\frac{\partial L}{\partial \psi}\right)\delta\psi, \tag{4}$$

which is the first-order linearization of (1), often referred to as the 'tangent linear equation' of the system. The Jacobian $(\partial L/\partial\psi)$ need not be autonomous since ψ can vary in time, in which case (4) represents a continuous linearization of (3) along the evolving trajectory defined by ψ.

To measure the growth of errors $\delta\psi$ in the system, it is convenient to define an error norm $E = \langle \delta\psi, \delta\psi \rangle$, where $\langle \ldots, \ldots \rangle$ represents a general inner-product. The growth of E over some forecast-period τ can be expressed in terms of a growth factor λ, whereby

$$\lambda = \frac{E(\tau)}{E(0)} = \frac{\langle \delta\psi(\tau), \delta\psi(\tau) \rangle}{\langle \delta\psi(0), \delta\psi(0) \rangle} = \frac{\langle R^* R \delta\psi(0), \delta\psi(0) \rangle}{\langle \delta\psi(0), \delta\psi(0) \rangle}, \tag{5}$$

where R is the 'propagator' of the tangent linear equation (4). The last term in (5) follows from the definition of the adjoint propagator R^* (Morse and Feshbach 1953), which is the propagator of the adjoint of the tangent linear equation, given by

$$-\frac{\partial \delta\psi^*}{\partial t} = \left(\frac{\partial L}{\partial \psi}\right)^* \delta\psi^*, \tag{6}$$

where the superscript * denotes an adjoint operator or variable. The form of $(\partial L/\partial\psi)^*$ in (6) depends on the inner product used to define E in (5). The perturbation $\delta\psi(0)$ for which λ takes on its maximum value corresponds to the fastest-growing eigenvector of the operator R^*R. The eigenvectors of R^*R are, by definition, the singular vectors of R which are orthogonal and form a complete set.

In general, $(\partial L/\partial\psi)$ is non-normal (i.e. $(\partial L/\partial\psi)^*(\partial L/\partial\psi) \neq (\partial L/\partial\psi)(\partial L/\partial\psi)^*$), in which case the modes of the coupled ocean–atmosphere system are non-orthogonal. Under these circumstances, disturbances can develop in the system that are favourably configured to undergo rapid transient growth, even in the absence of any growing modes. Because the modes are non-orthogonal, they have a non-zero projection on one another, so it is possible to superpose them to produce disturbances that initially grow more rapidly than the fastest growing mode of the system (Farrell 1982). As a result, initial-condition errors and model errors can grow rapidly in forecast models, contaminating the forecast and leading to a rapid fall in forecast skill. The singular vectors of R are a vehicle for this process, and for a given forecast-period τ, they represent the fastest-growing disturbances that can exist in the system before nonlinearity becomes important.

The technique for computing the singular vectors of the coupled model using the tangent linear coupled model and its adjoint, is described in detail by MK96. Here, we shall present only a brief description of the most important features of the Tangent Linear Coupled Model, hereafter referred to as the TLCM.

The first-order linearization δQ of the atmospheric-heating function (1), used to drive the atmospheric component of the TLCM, is given by

$$\delta Q = \begin{cases} \delta Q_c \text{ when } Q \neq -\overline{Q} \\ 0 \quad \text{otherwise,} \end{cases} \tag{7}$$

where $\overline{Q}$ is the observed climatological atmospheric-heating, and δQ_c is given by the linearized form of (1), namely

$$\begin{aligned} \delta Q_c = \frac{L_v \rho_4 c_E}{c_p \rho_2 I_1} \Big[& |\delta\mathbf{U}| \{ q_{\text{diff}}(\overline{T} + T') \} + (|\overline{\mathbf{U}}| + |\mathbf{U}|) \\ & \times \{ q_{\text{diff}}(\overline{T} + T' + \delta T') - q_{\text{diff}}(\overline{T} + T') \} \Big] \\ & + \frac{L_v I_2}{c_p \rho_2 I_1} \Big[\nabla \cdot \{ (\overline{q} + q)\delta\mathbf{U} \} + \nabla \cdot \{ \delta q (\overline{\mathbf{U}} + \mathbf{U}) \} \Big]. \end{aligned} \tag{8}$$

In (8), a δ-prefix denotes a perturbation in the TLCM to the variable indicated.

From (2), the first-order linearization of the SST anomaly used in the ocean component of the coupled model is given by

$$\frac{\partial \delta T'}{\partial t} = \underbrace{\gamma \delta h}_{\text{(i)}} - \underbrace{\theta \delta w \frac{\partial \overline{T}}{\partial z}}_{\text{(ii)}} - \underbrace{(\overline{u} + u)\frac{\partial \delta T'}{\partial x} - \delta u \frac{\partial (\overline{T} + T')}{\partial x}}_{\text{(iii)}} - \underbrace{\epsilon \delta T' + \kappa \frac{\partial^2 \delta T'}{\partial x^2}}_{\text{(iv)}}, \tag{9}$$

where

$$\gamma = \begin{cases} \eta \text{ if } |h| \leq h_{\max} \\ 0 \text{ otherwise} \end{cases} \tag{10}$$

and

$$\theta = \begin{cases} 1 & \text{if } |\Delta(\overline{w}+w) - \Delta(\overline{w})|\frac{\partial \overline{T}}{\partial z} > 0 \text{ and } |\Delta(\overline{w}+w) - \Delta(\overline{w})|\frac{\partial \overline{T}}{\partial z} \neq \overline{w}\frac{\partial \overline{T}}{\partial z} \\ 0 & \text{otherwise} \end{cases} . \quad (11)$$

Condition (10) reflects the fact that thermocline-depth perturbations δh do not influence SST when the thermocline nonlinearity is active (i.e. when the thermocline is very deep or very shallow). Similarly, condition (11) restricts the influence of vertical-velocity perturbations δw on SST to situations where there is upwelling in the mean basic state, and where upwelling anomalies w do not cause the mean upwelling $\overline{w}$ to be shut down or reversed. The validity and accuracy of linearizations such as (7), (10) and (11) were discussed and tested by MK96.

In the next section we shall often refer to the thermocline term (i), the upwelling term (ii) and the zonal advection term (iii) in (9) by the title letters T, U and A respectively.

For future reference, we note that, for the parameters used here, the eigenvalues of $\partial L/\partial \psi$ in (4) that describes the TLCM take the form of oscillations that are damped in time. This aspect of the coupled model is described in Part II.

4. The singular vectors of the observed seasonal cycle

We shall begin by examining the influence of each of the thermodynamic processes described by terms (i), (ii) and (iii) in the perturbation SST equation (9) on the structure and growth of the singular vectors (hereafter SVs) of the coupled model. The dissipation term (iv) was included in all our SV calculations. The year was divided into quarters starting with January–March (JFM), followed by April–June (AMJ), and so forth. The singular vectors of each quarter were computed, corresponding to $\tau = 3$ months in (5). This is the seasonal timescale over which forecast errors of ENSO are found to grow (Latif *et al.* 1994; Palmer and Anderson 1994). The sensitivity of the SVs to variations in τ will be discussed in Part II.

We find that for each combination of thermodynamic processes considered, the SV spectrum is dominated by one member. Table 1 shows the energy growth factors (i.e. the squares of singular values) of the dominant member of the SV spectrum computed during each quarter of the year for different combinations of the terms in (9). Only the observed

TABLE 1. Perturbation energy growth factors

Active thermodynamics	January to March	April to June	July to September	October to December
Thermocline term only (TSV)	4.0	6.5	4.3	3.8
Upwelling only (USV)	4.4	5.4	8.4	6.4
Zonal advection only (ASV)	5.5	3.2	7.5	7.7
All terms (TAUSV)	19.6	20.0	47.9	34.5
Thermocline term + upwelling (TUSV)	8.8	15.8	15.5	11.5
Thermocline term + zonal advection (TASV)	7.9	8.5	11.6	10.7
Zonal advection + upwelling (AUSV)	15.6	9.9	37.1	28.1

The perturbation energy growth factors λ of the fastest growing member of the singular vector spectra which result when the thermodynamic processes indicated are active in the perturbation SST Eq. (9). The optimal growth time in each case is 3 months, and λ are shown for the singular vectors which result during each quarter of the year in the presence of the observed seasonal cycle only.

seasonal cycle is included in these calculations in the TLCM and adjoint TLCM, and the background anomaly fields of the coupled model are identically zero everywhere (i.e. $T' = q = \mathbf{U} = w = 0$ in (8) and (9)). For convenience, we refer to the SVs computed with the thermocline and dissipation terms alone as TSV, those with the zonal advection and dissipation terms alone as ASV, and those with the upwelling and dissipation terms alone as USV. Similarly, different combinations of thermodynamic processes will be referred to by the title letters (T, U and A) of the processes which are active, so that when all processes are active, the corresponding SVs will be referred to as TAUSV, and so on.

The first row in Table 1 shows the perturbation-energy growth-factors λ for the dominant TSVs during each quarter of the year. The highest value occurs during the AMJ quarter. (The dynamics responsible for the growth of the TSVs were examined in detail by MK96.) The second row in Table 1 shows λ for the dominant USV which has its maximum value during JAS. The ASVs (third row in Table 1) also grow most rapidly during the latter half of the year. The growth factors of USV and ASV are generally somewhat larger than those of TSV at most times of the year except during the AMJ quarter, when λ for the ASV has its minimum value while TSV has its maximum value. When all processes are active together in (9), Table 1 (fourth row) shows that the TAUSVs can grow very rapidly, with maximum growth during the JAS quarter some 6–10 times greater than λ for TSV, ASV or USV.

The bottom three rows in Table 1 show the values of λ for all possible combinations of terms (i)–(iii) with dissipation in (9) when they operate in pairs (i.e. TUSV, TASV and AUSV). Values of λ range from 7.9 for TASV during JFM, to 37.1 for AUSV during JAS. Inspection of Table 1 shows that there is no simple relationship between the values of λ of TSV, ASV and USV, and the values that result from different combinations of processes T, A and U. To understand why this is so, consider the propagator of the coupled system associated with each term in (9). By virtue of the linearity of the TLCM, we can define a propagator for the system which arises when each term in (9) operates alone with dissipation. Hence, we will use R_{T} to denote the propagator arising from terms (i) and (iv) alone in (9), R_{U} to denote the propagator arising from terms (ii) and (iv) alone in (9), and R_{A} for that arising from terms (iii) and (iv) alone. The energy growth-factors λ of TSV, ASV and USV are therefore the eigenvalues of $R'_{\mathrm{T}}R_{\mathrm{T}}$, $R'_{\mathrm{A}}R_{\mathrm{A}}$ and $R'_{\mathrm{U}}R_{\mathrm{U}}$ respectively, where a prime $'$ denotes the matrix transpose. The singular values of TASV, for example, are the eigenvalues of

$$R'_{\mathrm{TA}}R_{\mathrm{TA}} = (R_{\mathrm{T}} + R_{\mathrm{A}})'(R_{\mathrm{T}} + R_{\mathrm{A}}) = R'_{\mathrm{T}}R_{\mathrm{T}} + R'_{\mathrm{T}}R_{\mathrm{A}} + R'_{\mathrm{A}}R_{\mathrm{T}} + (R'_{\mathrm{A}}R_{\mathrm{T}})'. \tag{12}$$

The matrix sum $R'_{\mathrm{A}}R_{\mathrm{T}} + (R'_{\mathrm{A}}R_{\mathrm{T}})'$ is by definition symmetric, so the symmetry of the entire matrix sum in (12) is assured. Clearly, there is no simple relation between the eigenvalues of $R'_{\mathrm{T}}R_{\mathrm{T}}$, $R'_{\mathrm{A}}R_{\mathrm{A}}$ and those of $R'_{TA}R_{TA}$. We shall return to this aspect of SV growth in Part II. Table 1 indicates, however, that the seasonal dependencies of the singular values of R_{T}, R_{A} and R_{U} appear to combine constructively. To understand these seasonal dependencies for each class of SVs, we must examine their energetics in detail.

The domain-integrated, non-dimensional, perturbation-energy of the coupled system is given by

$$\begin{aligned} E(t) &= \int\int \frac{1}{2} m_{\mathrm{a}}(\widehat{\delta U}^2 + \widehat{\delta V}^2 + \widehat{\delta\Phi}^2/c^2)\mathrm{d}x\mathrm{d}y \\ &\quad + \int\int \frac{1}{2} m_{\mathrm{o}}(\widehat{\delta u}^2 + \widehat{\delta h}^2)\mathrm{d}x\mathrm{d}y \\ &= \int\int E_{\mathrm{a}}\mathrm{d}x\mathrm{d}y + \int\int E_{\mathrm{o}}\mathrm{d}x\mathrm{d}y, \end{aligned} \tag{13}$$

where $\widehat{\delta U} = \delta U/c_o$, $\widehat{\delta V} = \delta V/c_o$, $\widehat{\delta \Phi} = \delta \Phi/c_o^2$, $\widehat{\delta u} = \delta u/c_o$, $\widehat{\delta h} = g'\delta h/c_o^2$ and $c = c_a/c_o$; $\delta\Phi$ is the perturbation geopotential height in the atmosphere; c_o and c_a are the phase speeds of equatorial Kelvin waves in the ocean and atmosphere respectively, and the integrations are over all atmospheric and oceanic grid-boxes with masses m_a and m_o. From here on, we shall drop the circumflex marks, and all variables will be assumed to be non-dimensional unless otherwise stated. The atmospheric and oceanic components of perturbation energy in each model grid-box are denoted E_a and E_o respectively in (13). The oceanic component E_o is dominated by the input of energy into the ocean by the surface perturbation-wind field, and will not be considered further.

From MK96, the equation governing the time development of $\int\int E_a dx dy$ is given by

$$\begin{aligned}\int\int E_a dx dy = &\underbrace{-\int\int \frac{\delta\Phi \delta T'}{4c^2} dx dy}_{\text{Direct thermal}} \\ &\underbrace{-\frac{A}{4\epsilon c^2}\int\int \delta\Phi\{\delta W q_{\text{diff}} + \overline{W}\delta q_{\text{diff}}\} dx dy}_{\text{Surface latent heat}} \\ &\underbrace{-\frac{B}{4\epsilon c^2}\int\int \delta\Phi \nabla\cdot(\overline{q}\delta\mathbf{U}) dx dy - \frac{B}{4\epsilon c^2}\int\int \delta\Phi\nabla\cdot(\delta q\overline{\mathbf{U}}) dx dy}_{\text{Moisture flux convergence}},\end{aligned} \tag{14}$$

where $A = L_v\rho_4 c_E/c_p\rho_2 I_1$ and $B = L_v I_2/c_p\rho_2 I_1$. The globally integrated atmospheric perturbation-energy budget consists of contributions from direct thermal forcing, surface latent-heating, and latent-heat release associated with moisture-flux convergence. The moisture-flux convergence term has two components in (14); one term is associated with the basic-state specific humidity $\overline{q}$ and the other with the basic-state atmospheric circulation $\overline{\mathbf{U}}$. MK96 have shown that for the TSV of Table 1, most of the error growth and seasonal variation in λ arises from the first of the moisture-flux-convergence terms in (14). Furthermore, MK96 showed that it is the component $\delta E_{mc} = -B\delta\Phi\overline{q}\nabla\cdot\delta\mathbf{U}/4\epsilon c^2$ of (14) which dominates the perturbation-energy budget. This term arises from convergence of basic-state humidity $\overline{q}$ by the perturbation wind $\delta\mathbf{U}$. Detailed energetic analyses, such as those of MK96, have revealed that δE_{mc} is the dominant term in the atmospheric perturbation-energy budgets of all the classes of SVs in Table 1. To illustrate this, Table 2 shows the contribution of each term in (8) to the atmospheric perturbation-energy budget over the tropical Pacific Ocean west of 150°W for each class of SV in Table 1. We shall demonstrate shortly that this is the region where all the SVs have their centres of action. Table 2 shows $\sum_{i=1}^{4}\int\int\int \chi dx dy dt/4$, where χ represents the contribution of each individual term in (8) to the total perturbation-energy; the space integrals are over the region 120°E–150°W, 30°S–30°N; the time integral is over the optimal growth-time $\tau = 3$ months; and the summation is over all quarters of the year where $i = 1 \equiv$ JFM, $i = 2 \equiv$ AMJ, and so on. Table 2 clearly shows that $\delta E_{mc} = -B\delta\Phi\overline{q}\nabla\cdot\delta\mathbf{U}/4\epsilon c^2$ dominates the perturbation-energy budget for each class of SV. As shown by MK96, much of the behaviour of the TSVs can be understood by analysing δE_{mc}. Therefore, from here on, we shall concentrate on the dynamics of the system that govern the growth of δE_{mc}. In the ensuing discussion, perturbation-energy growth is taken to be synonymous with error growth in the model.

Figure 1 shows time series of $\int\int E_a dx dy$ and $\int\int \delta E_{mc} dx dy$ for TSV, ASV, USV and TAUSV during each quarter of the year. The general characteristics of the values of λ

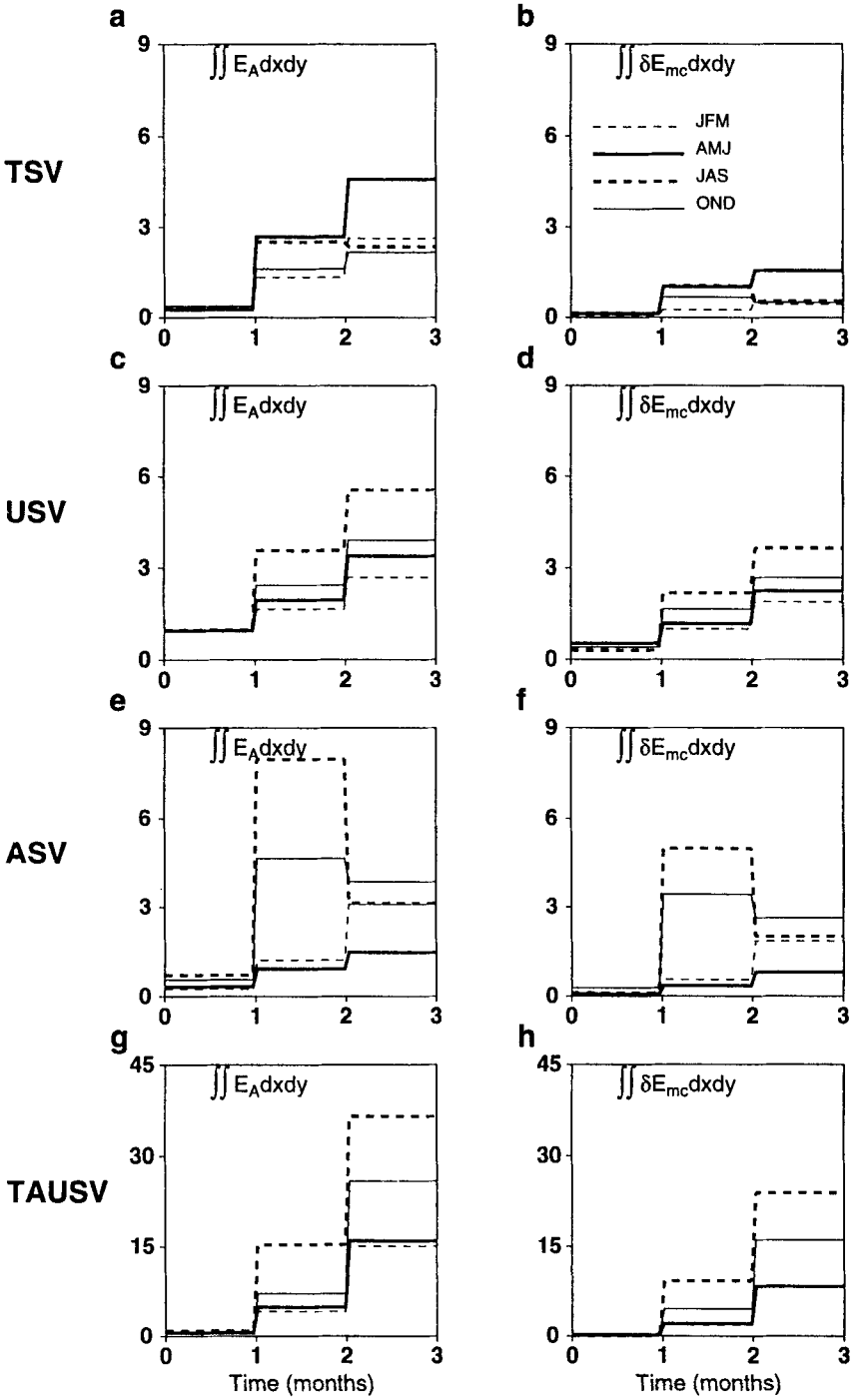

Figure 1. Time series of the non-dimensional atmospheric perturbation-energy E_a and the dominant moisture-flux-convergence term δE_{mc}, both globally integrated, for TSV, USV, ASV and TAUSV during each quarter of the year. An optimal growth time of 3 months is assumed in each case. See text for acronyms.

TABLE 2. CONTRIBUTIONS TO THE PERTURBATION HEATING FUNCTION

	$-\overline{q}\nabla\cdot\delta\mathbf{U}$ (δE_{mc})	$-\delta T'$	$-\delta\mathbf{U}\cdot\nabla\overline{q}$	$-\overline{\mathbf{U}}\cdot\nabla\delta q$	$-\delta q\nabla\cdot\overline{\mathbf{U}}$	$-(\delta W q_{diff}+\overline{W}\delta q_{diff})$
TSV	1.4	0.7	0.001	0.2	0.06	0.1
USV	4.7	1.5	−0.05	0.3	0.3	0.3
ASV	4.4	1.4	−0.01	0.4	0.2	0.3
TAUSV	19.8	6.8	−0.3	1.5	1.0	1.5

If we denote by χ the contribution of each individual term in the perturbation heating function (8) to the total perturbation energy, then this table shows $\sum_{i=1}^{4}\int\int\int\chi\,dx\,dy\,dt/4$ where the space integrals are over the region 120°E – 150°W, 30°S – 30°N and the time integral is over the optimal growth time $\tau = 3$ months. The summation is over all quarters of the year, where $i = 1 \equiv$ January, February and March, $i = 2 \equiv$ April, May and June, and so on. The terms used for χ in the above expression are indicated along the top of the table, where the multiplying factors outside the integrals of (14) and the factors $\delta\Phi$ have been ommited for clarity. The second column labelled $-\delta T'$ shows the contribution of the direct thermal forcing term (cf. Eq. (14)) to the perturbation energy budget.

in Table 1 are reflected in the growth of E_a and δE_{mc} in Fig. 1. During the JAS quarter (and to a lesser extent OND), there is a tendency for $\int\int\delta E_{mc}dxdy$ to attain its maximum value around mid-quarter for TSV and ASV before decreasing again. This particular feature is the result of error growth near the Philippines during the onset of the NE Asian monsoon when conditions there are favourable for the growth of TSV and ASV. This will be discussed in more detail shortly.

We shall now examine the SVs of each thermodynamic process in (9) and so their influence on perturbation growth in the coupled model. Each process will be considered individually, to give us a clear understanding of the dynamics of error growth in each case and the influence of the seasonal cycle. From these individual studies we can then understand the characteristics of perturbation growth when different thermodynamic processes influence SST in tandem.

(*a*) *The influence of thermocline dynamics on SV growth*

The seasonal variation in values of λ for TSV was examined in detail by MK96 and found to result primarily from seasonal variations in δE_{mc}. They showed that, for energy growth via δE_{mc}, two conditions must be met simultaneously: (A) conditions must be favourable for deep penetrative convection (i.e. $\overline{Q} \neq 0$), which is the case where $\overline{T} \geqslant 28°C$, and (B) $\delta T'$ must be relatively sensitive to γ in (9). Condition (B) is necessary because, for δE_{mc} to be large, a perturbation-wind field $\delta\mathbf{U}$ with non-zero divergence (i.e. $\nabla\cdot\delta\mathbf{U} \neq 0$) is required. Such a wind field will develop in response to $\delta T'$ and to the west of the SST perturbation. The growth of $\int\int\delta E_{mc}dxdy$ will be greatest when the area over which conditions (A) and (B) are simultaneously satisfied is largest. For TSV, (A) and (B) are satisfied simultaneously only in the central Pacific Ocean. The seasonal cycle of $\overline{T}$ in this region has a strong influence on δE_{mc}, with λ being largest in boreal spring and early summer when the warm pool of the west Pacific has its greatest eastward extension. At this time of year, the geographical area over which (A) and (B) are satisfied is greatest, hence $\int\int\delta E_{mc}dxdy$ and λ have their largest values then.

Figure 2 shows maps of δE_{mc}, superimposed on the climatological SST, $\overline{T}$, for the fastest-growing TSV which results during the AMJ quarter. Values of δE_{mc} are shown only over the tropical Pacific since elsewhere they are negligible. The area over which conditions (A) and (B) are satisfied simultaneously is delineated by the 28°C isotherm and the vertical dashed line where $\eta_C = \eta_W$ in the central Pacific. The area bounded by these

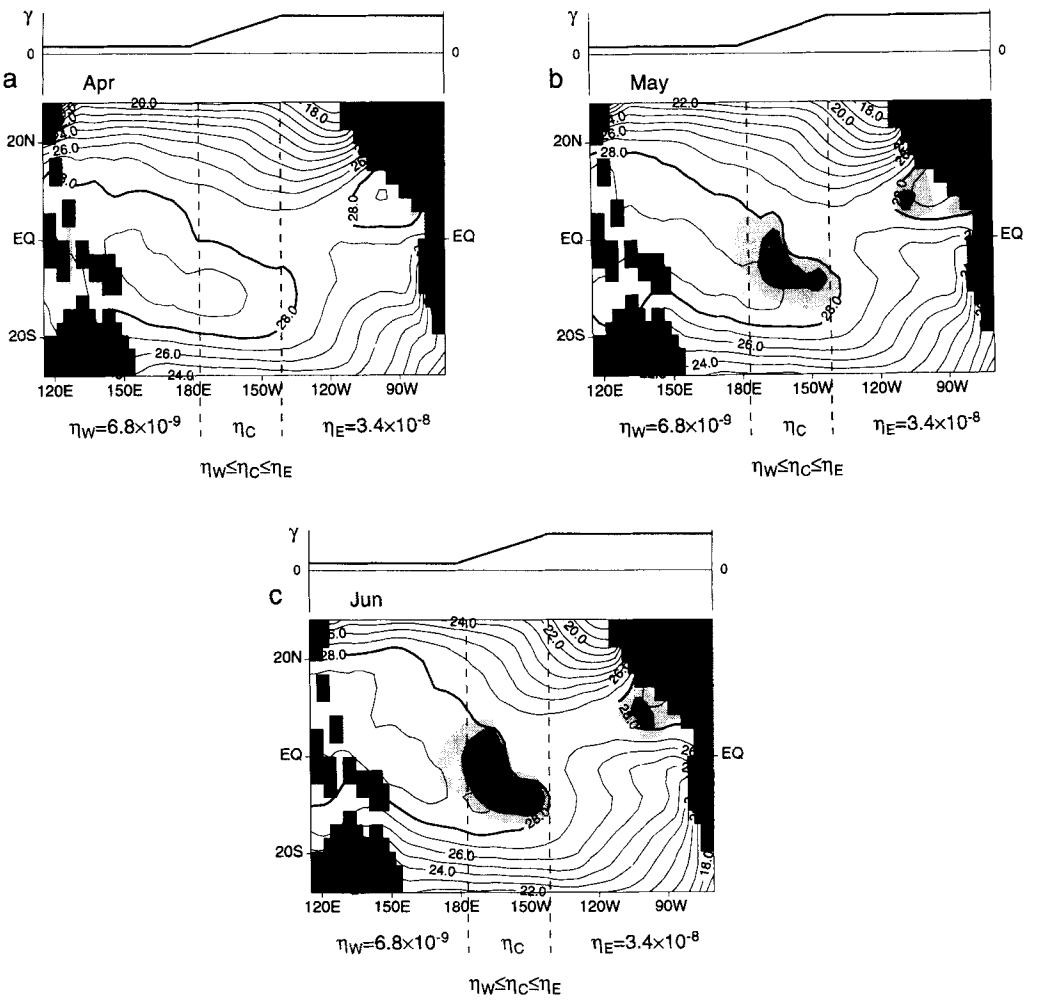

Figure 2. Contour maps of the observed monthly mean sea surface temperature (SST) in the tropical Pacific Ocean during April, May and June (AMJ). Superimposed on each map are shaded contours of the dominant moisture-flux-convergence term δE_{mc} for the fastest growing singular vector computed with the thermocline term alone (TSV) for the AMJ quarter. Also shown are values of η and profiles of γ used in (9) in each region of the model. The contour interval for SST is 1°C, and a change in grey scale for δE_{mc} corresponds to an interval of 1.5×10^{-2} non-dimensional units. The 28°C isotherm is highlighted.

curves is largest during AMJ, and, by the end of the quarter, δE_{mc} has expanded to fill most of this area. Note also the region of growth of δE_{mc} in the east Pacific just north of the equator where $\overline{T} \geq 28°C$, and where (A) and (B) are also satisfied at the same time.

Dynamical arguments similar to those applied to TSV can be invoked to explain the seasonal variations in λ for USV and ASV. Indeed, condition (A) above must be met for all SVs of the perturbation-energy norm (13) of the coupled model, so we expect the seasonal cycle in SST to play an important role in modulating λ, regardless of which thermodynamic processes operate in (9).

(*b*) *The influence of equatorial upwelling on SV growth*

For USV, error growth via δE_{mc} occurs when, in addition to condition (A), the following condition is also satisfied: (C) $\delta T'$ is sensitive to equatorial-upwelling perturbations

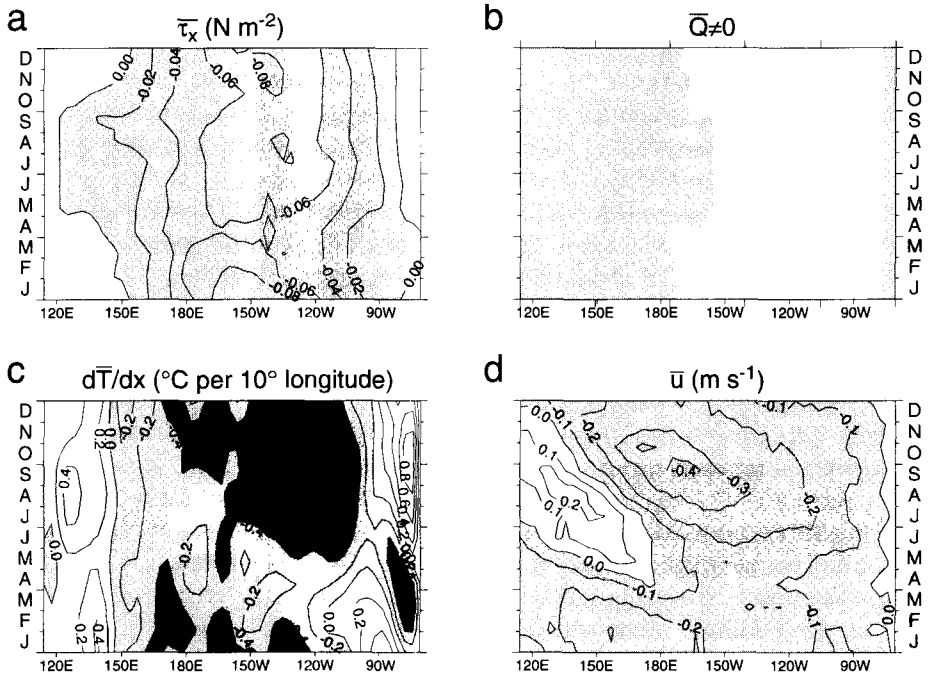

Figure 3. Hovmöller diagrams: (a) the observed monthly mean zonal wind stress $\overline{\tau}_x$ along the equator. The contour interval is 0.02 N m^{-2} and regions of winds from the east are shaded; (b) grid points of the coupled model at which the mean atmospheric heating $\overline{Q} \neq 0$ at the equator. Shading indicates where $\overline{Q} \neq 0$; (c) the zonal gradient of observed monthly mean SST, $\partial\overline{T}/\partial x$. Light shading indicates where $0 \geqslant \partial\overline{T}/\partial x \geqslant -0.4$°C per 10° of longitude; dark shading indicates regions where $\partial\overline{T}/\partial x < -0.4$°C per 10° of longitude. The contour interval is 0.2°C per 10° of longitude; (d) the monthly zonal ocean-current $\overline{u}$. The contour interval is 0.1 m s^{-1}, and regions of flow towards the west are shaded.

δw. According to (11), perturbations δw can influence $\delta T'$ only where $\overline{w} \geqslant 0$ (i.e. where there is mean upwelling). The mean vertical velocity $\overline{w}$ at the equator is computed as described in section 2 by assuming that there is a shear between the surface mixed-layer and the deep ocean (Zebiak and Cane 1987; Phlips 1987; Neelin 1991). In this way, $\overline{w}$ can be computed from the observed, climatological, wind stress $\overline{\tau}$ as described by K93, and is given at the equator by

$$\overline{w} = \frac{1}{\rho_0 \alpha}\left[\nabla \cdot \overline{\tau} - \frac{\beta}{\alpha}\overline{\tau}_x\right], \tag{15}$$

where ρ_0 is the density of the ocean, α is a strong damping coefficient (0.5 d^{-1}) and $\overline{\tau}_x$ is the zonal component of climatological wind stress along the equator. Typically, the second term in (15) is an order of magnitude larger than the first, so that to a good approximation $\overline{w}$ is proportional to $-\overline{\tau}_x$ at the equator. Figure 3(a) shows a Hovmöller diagram of $\overline{\tau}_x$ along the equator in the Pacific Ocean; note that $\overline{w} \geqslant 0$ where $\overline{\tau}_x \leqslant 0$.

Conditions (A) and (C), favourable for the growth of δE_{mc} for USV, will be satisfied simultaneously in the western and central Pacific only where $\overline{T} \geqslant 28$°C and $\overline{w} \geqslant 0$. As a guide to condition (A), Fig. 3(b) shows a Hovmöller diagram of the area over which deep penetrative convection can occur at the equator (i.e. $\overline{Q} \neq 0$). Figure 3(a) shows that $\overline{w} \geqslant 0$ at the equator across the entire Pacific during JAS, so $\int\int \delta E_{\mathrm{mc}} \mathrm{d}x\mathrm{d}y$ and λ for USV have their largest values at this time of year. In addition, the region over which $\overline{Q} \neq 0$ also occupies the largest area along the equator at this time (Fig. 3(b)). At other times

of the year $\overline{w} \leqslant 0$ in the western Pacific, creating conditions that are unfavourable for perturbation-energy growth.

Figure 4 shows maps of δE_{mc} in the tropical Pacific, superimposed on $\overline{T}$, for the USVs of the JAS and JFM quarters, when λ has its maximum and minimum values, respectively, in row 2 of Table 1. Also shown in each panel of Fig. 4 is the profile of $\overline{w}$ along the equator. The area bounded by the 28°C isotherm and $\overline{w} \geqslant 0$ at the equator is that in which conditions (A) and (C) are satified simultaneously. During JAS, $\overline{w}$ is fairly steady and the upwelling region has its maximum extension westwards. In addition, the west Pacific warm pool spans the equator in the central Pacific and, over time, the warm-water pool pushes further east to the north and south of the equator. To achieve maximum growth during this quarter, the USV sets up an initial disturbance in the central Pacific causing δE_{mc} to begin growing in July at the easternmost edge of the 28°C isotherm. Upwelling perturbations δw cause SST perturbations $\delta T'$ to propagate westwards, so, as time advances, δE_{mc} grows towards the west to fill the region near the equator where $\overline{T} \geqslant 28$°C. These large values of δE_{mc} are maintained by perturbation-divergent Rossby-waves in the atmosphere which are driven by, and reside west of, SST perturbations $\delta T'$.

During JFM, when the dominant USV has its slowest growth rate, $\overline{w}$ is increasing in the central Pacific where (A) and (C) are satisfied, and $\overline{w} \leqslant 0$ in the west. In addition, the warm-water pool lies mainly south of the equator, and at the equator does not extend far into the region where $\overline{w} > 0$. As a result, the area over which USV is able to sustain rapid growth is smaller than at other times of the year, as δE_{mc} grows towards the west, as shown in Fig. 4(d,e,f).

(c) *The influence of zonal advection on SV growth*

For ASV, error growth via δE_{mc} is most favourable when condition (A) and the following condition are satisfied simultaneously: (D) $\delta T'$ is sensitive to perturbation zonal advection. Perturbation zonal advection occurs via term (iii) in (9) which is composed of two parts. These are the advection of mean SST $\overline{T}$ by perturbation currents δu and the advection of SST perturbations $\delta T'$ by the mean current $\overline{u}$. At the equator between about 140°E and 100°W, $\partial \overline{T}/\partial x \leqslant 0$ for much of the year. The east–west gradient in $\overline{T}$ is a minimum over much of the tropical Pacific during boreal spring as shown in Fig. 3(c) which shows a Hovmöller diagram of $\partial \overline{T}/\partial x$ along the equator. The mean current $\overline{u}$ also varies considerably throughout the year and shows a pronounced seasonal cycle. Figure 3(d) shows a Hovmöller diagram of $\overline{u}$ along the equator over the course of a year. For much of the year, $\overline{u} \leqslant 0$ across the entire Pacific (i.e. the South Equatorial Current) in response to the easterly trade winds. Around April, $\overline{u}$ changes sign just west of the date line, and becomes eastward further west as the year advances. This reversal of the current is associated with off-equatorial winds that excite oceanic Rossby-waves, which explains the westward propagation evident in $\overline{u}$ of Fig. 3(d). Conditions (A) and (D) can be satisfied simultaneously only in the western and central Pacific.

Figure 5 shows maps of δE_{mc} superimposed on contours of $\overline{T}$ for the ASVs of the OND and AMJ quarters when the values of λ in row 3 of Table 1 are a maximum and minimum respectively. Also shown in Fig. 5 are plots of $\overline{u}$ along the equator during each month. During OND, conditions (A) and (D) yield conditions that are favourable for the growth of δE_{mc} in two regions centred in the central and far western Pacific. In the central Pacific, $\overline{u} < 0$, so SST perturbations $\delta T'$ will be advected by $\overline{u}$ towards the west. Advection of $\overline{T}$ by velocity perturbations δu will tend to produce westward propagation also, but in general this is the weaker of the two advection terms in (9). To attain rapid growth in the central Pacific, the ASV initiates a perturbation near the eastern edge of the 28°C isotherm, causing δE_{mc} to grow here. Over time, δE_{mc} grows westward as $\delta T'$ is

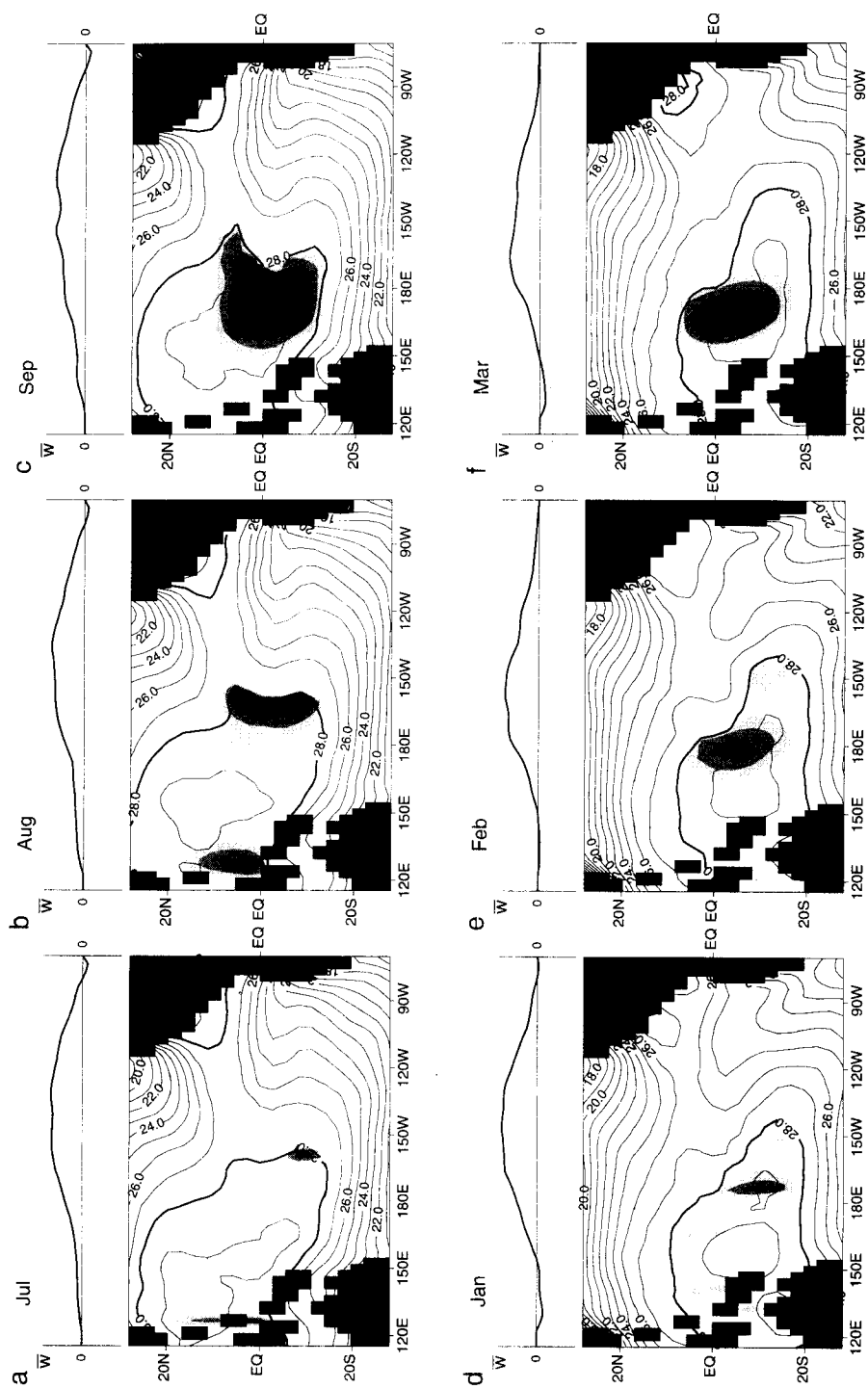

Figure 4. Contour maps of the observed monthly mean SST in the tropical Pacific Ocean during July, August and September (JAS), and January, February and March (JFM). Superimposed on each map are shaded contours of δE_{mc} for the fastest-growing 'upwelling' singular vector (USV) during the JAS and JFM quarters. Also shown are profiles of the monthly mean vertical velocity $\overline{w}$ at the equator. The contour interval for SST is 1°C, and a change in grey scale for δE_{mc} corresponds to an interval of 1.5×10^{-2} non-dimensional units. The 28°C isotherm is highlighted.

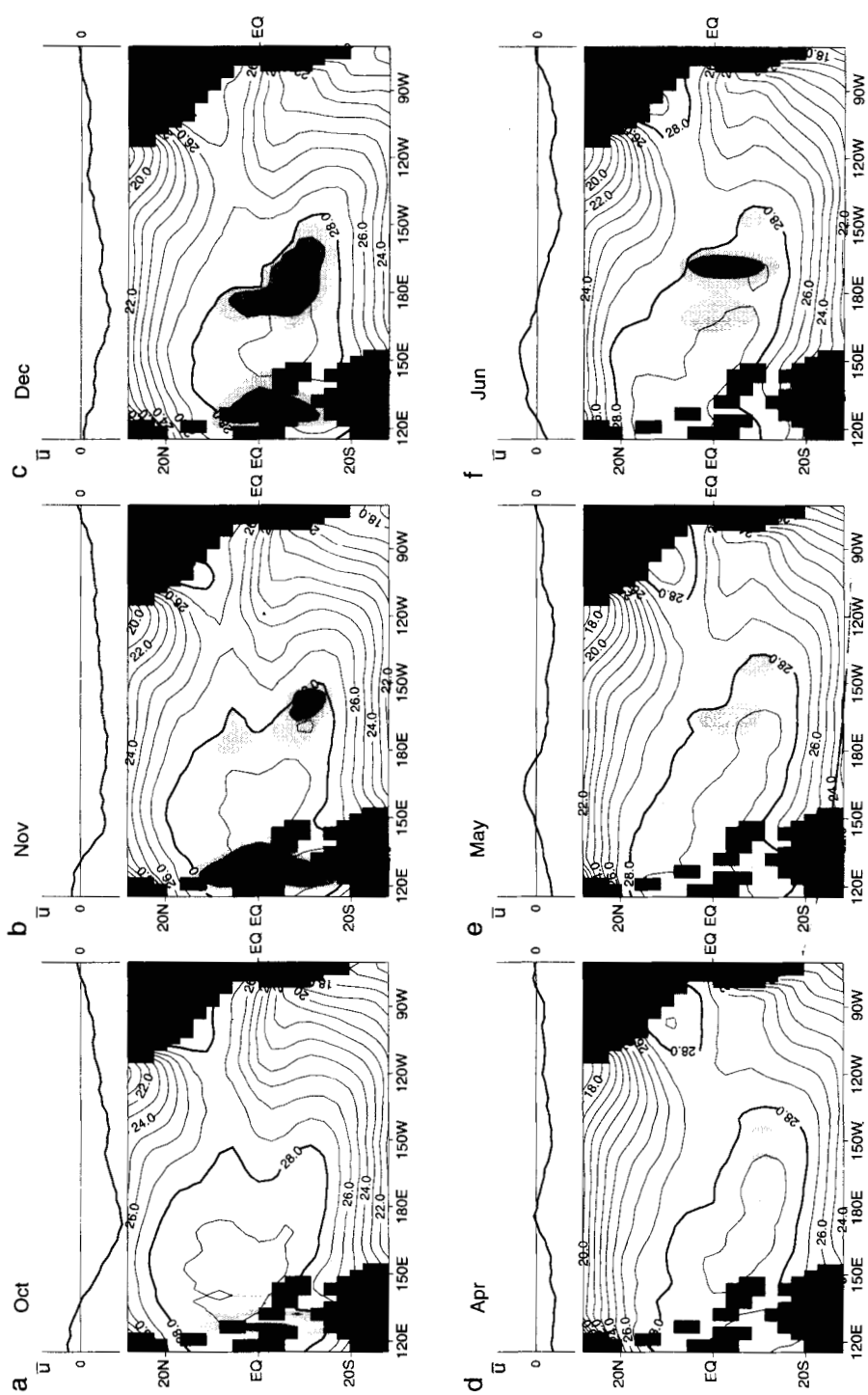

Figure 5. Contour maps of the observed monthly mean SST in the tropical Pacific Ocean during October, November and December (OND) and April, May and June (AMJ). Superimposed on each map are shaded contours of δE_{mc} for the fastest growing 'advection' singular vector (ASV) during the OND and AMJ quarters. Also shown are profiles of the monthly mean zonal ocean current $\bar{u}$ at the equator. The contour interval for SST is 1°C, and a change in grey scale for δE_{mc} corresponds to an interval of 1.5×10^{-2} non-dimensional units. The 28°C isotherm is highlighted.

advected westward into the warm-pool region. In the far western Pacific, $\overline{u} > 0$, in which case δE_{mc} can grow as $\delta T'$ is advected eastward across the warm pool by $\overline{u}$. Error growth near the Philippines is very rapid during November (cf. Fig. 1(e,f)) because of the onset of the north-east Asian monsoon which creates winds with a strong eastward component just south of the equator, and areas of strong convergence to the north which enhance the atmospheric heating δQ. A similar situation also arises during JAS, but to a lesser extent, during the height of the south-east Asian monsoon. (As noted earlier, conditions favourable for energy growth near the Philippines can also occur at certain times of the year associated with TSV. Thermocline perturbations cause eastward propagation of SST perturbations (see Neelin 1991) and so δE_{mc} can grow eastward from the Philippines region if atmospheric conditions are favourable.) During AMJ, Fig. 3(c,d) shows that $\partial \overline{T}/\partial x$ and $\overline{u}$ have their minimum values: these months are relatively unfavourable for the growth of ASV via δE_{mc}, as shown in Fig. 5(d,e,f).

(*d*) *The combined influence of all thermodynamic processes on SV growth*

When the different thermodynamic processes in (9) are combined, conditions (A) to (D) must still be met for growth via δE_{mc}, depending on which processes are active. The resulting SVs will not be a simple linear combination of TSV, ASV and USV, because cross-product terms result from the propagators for each process, as in (12). Experiments, in which different linear combinations of TSV, ASV and USV were used to initialize the TLCM, confirm this (not shown). The seasonal cycle in $\overline{T}$, $\overline{\tau}_x$ and $\overline{u}$, however, can act to give very rapid growth if the relative phase between these fields makes the growth of δE_{mc} favourable. Figure 3 shows that, during JAS over the west Pacific warm-pool, $|\overline{u}|$ is large and $\overline{\tau}_x$ induces upwelling, while in the central Pacific $\overline{T} \geqslant 28°\mathrm{C}$ over large areas to the north and south of the equator, so conditions are favourable for the growth of δE_{mc} by all three thermodynamic processes, and perturbation-energy growth is rapid. During this time of year, values of λ for TAUSV show that errors in the coupled system can grow by a factor of almost 50 (cf. row 4 of Table 1).

The structure of the fastest-growing TAUSV during the JAS quarter is shown in Fig. 6 which shows the evolution of $\delta T'$, δh, δu, δw and $\delta \mathbf{U}$. The perturbation SST $\delta T'$ of Fig. 6(a) has a structure that is initially dominated by small-scale features in July. This aspect of the perturbation-energy norm SVs was discussed in detail by MK96, and is associated with the structure of the weight matrix $\mathbf{S}$ which must be included in (5) to yield the perturbation energy norm (13)*. In this case (5) becomes a generalized eigenvalue equation. The weight matrix $\mathbf{S}$ has a blocked structure, with separate blocks that are associated with the perturbation energy of the atmosphere and ocean (cf. (13)). The atmospheric block of $\mathbf{S}$ causes its eigenvalues ν to span five orders of magnitude, the smallest of which are associated with short-wavelength eigenvectors. The solution of (5) requires an inversion of $\mathbf{S}$; this causes any projection that a vector $\delta\psi$ might have on to these short-wavelength eigenvectors to be amplified by a factor of $1/\nu$ which can be large; hence the appearance of these eigenvectors in the TAUSV of Fig. 6(a). However, the analytic solutions of Gill (1980), for a similar atmospheric model, show that a decrease in the zonal scale of SST perturbations (and hence perturbation atmospheric heating) is accompanied by a decrease in the total perturbation-energy of the atmospheric response. Therefore, the small scale variations in the initial $\delta T'$ of Fig. 6(a) are inconsequential to the perturbation-energy

* The non-dimensionalized perturbation state-vector $\delta\psi$ of the coupled model is given by $\delta\psi^T = (R_{\mathrm{d}}\delta T'/c_{\mathrm{o}}^2, \delta u/c_{\mathrm{o}}, g'\delta h/c_{\mathrm{o}}^2)$ where R_{d} is the gas constant for dry air and g' the reduced gravity of the upper ocean. The total-energy norm E is given by (13) and can be expressed as $E = \delta\psi^T \mathbf{S} \delta\psi$. The weight matrix $\mathbf{S}$ contains information about the grid-box masses m_{a} and m_{o}, and the atmospheric dynamics that relate the perturbation wind $\delta\mathbf{U}$ and geopotential height $\delta\Phi$ to $\delta T'$.

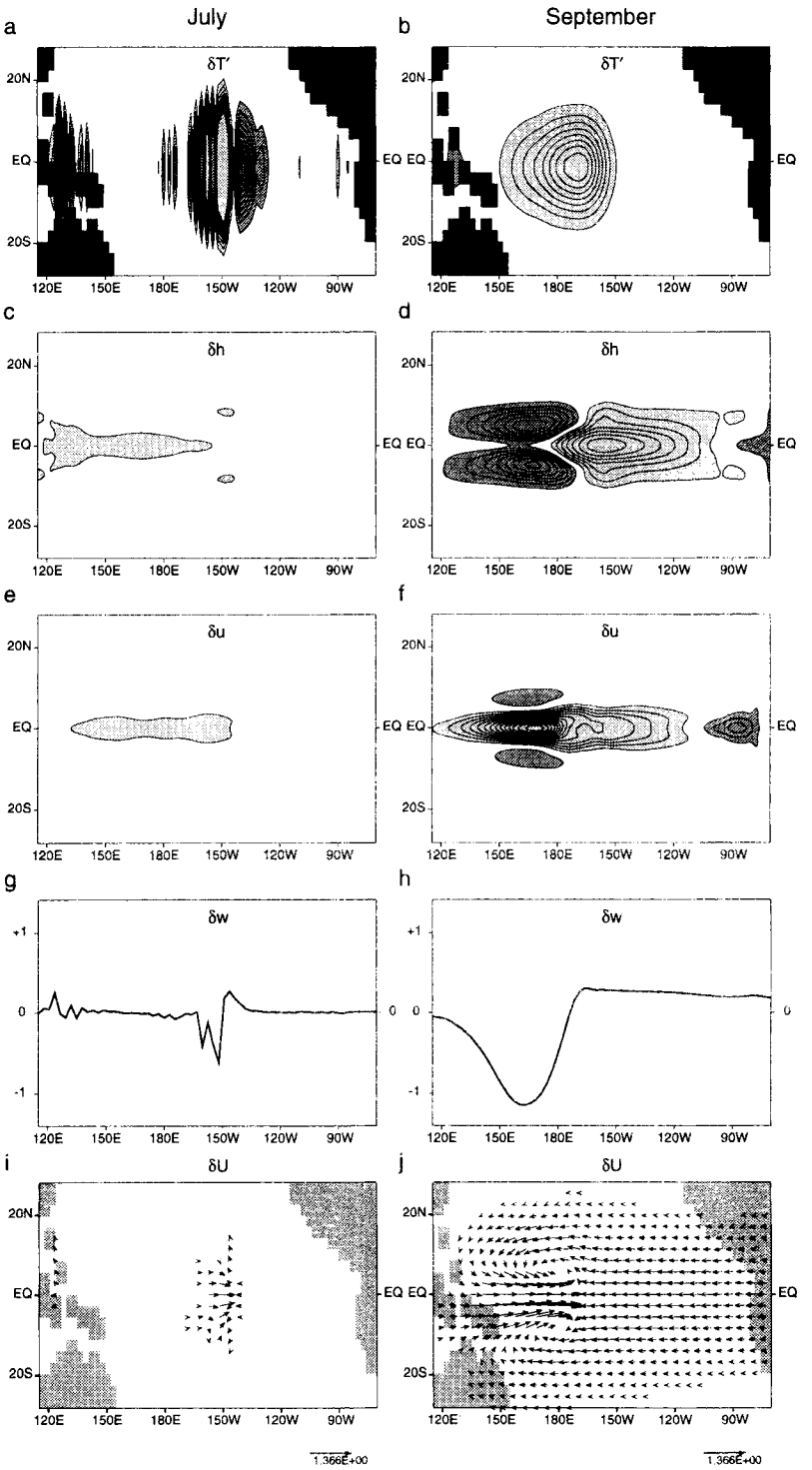

Figure 6. The structure of the fastest growing 'all terms' singular vector (TAUSV) over the tropical Pacific, during the July, August and September (JAS) quarter. Maps detailing the structure of the perturbation SST (δT), perturbation thermocline depth (δh), perturbation zonal ocean current (δu), equatorial perturbation vertical velocity (δw), and vectors of the perturbation wind ($\delta \mathbf{U}$) are shown at the end of July and September. Light shading represents positive values of each quantity, while dark shading indicates negative values. Because the SVs are the result of a linear analysis, the scaling of the various fields is arbitrary.

growth of the SV, as demonstrated by MK96, and they are quickly dissipated as the SV evolves. By September, the perturbation SST field is smooth, and westward propagation of the large-scale component of $\delta T'$ is evident.

The cause of error growth via δE_{mc} is evident from Fig. 6 when all thermodynamic processes are active in the upper ocean. Thermocline perturbations δh (Fig. 6(c,d)), zonal-velocity perturbations δu (Fig. 6(e,f)), and upwelling perturbations δw (Fig. 6(g,h)) all conspire to give growth of $\delta T'$ in the central and western Pacific. As $\delta T'$ evolves, perturbation winds $\delta \mathbf{U}$ develop in response. The moisture-convergence term δE_{mc} grows due to the presence of short atmospheric Rossby-waves that promote convergent circulations that are clearly visible in Fig. 6(j) as a pair of cyclones spanning the equator near the date line. These divergent atmospheric circulations promote moisture convergence which creates atmospheric heating δQ through penetrative convection, that in turn produces an intensification of the wind field. The increasing wind-perturbations drive further thermocline-displacements δh, changes in the ocean circulation δu and δw, and a positive-feedback loop results leading to the rapid transient growth of perturbations in the system. As shown in Part II, this process can persist for periods in excess of 24 months.

The wind-field structure, circulation and behaviour of the dominant SV is relatively insensitive to the upper-ocean thermodynamics active in (9). The final structures of TSV, USV and ASV wind-fields, after optimum growth has been achieved (not shown), are very similar to that of TAUSV shown in Fig. 6. This suggests that, in the tropics, the coupled system has a preferred response which the thermodynamics controlling SST produces, regardless of which of the processes are operating in the mixed layer. We shall discuss this aspect of the SVs further, in section 6.

5. The possible influence of the observed ENSO cycle on SV growth

Coupled models display tropical interannual variability that differs considerably from model to model (Neelin *et al.* 1992), and it is probably fair to say that no coupled model yet simulates satisfactorily the development of the observed ENSO signal, or the different characteristics of individual ENSO episodes. In addition to the work of MK96, SVs of the coupled system have been studied by Chen *et al.* (1997) and Xue *et al.* (1997) using the model of Zebiak and Cane (1987). Like MK96, these investigators have examined the influence of the model ENSO cycle on SV growth. While there are some similarities between the findings of these three studies, there are many differences between the two models used and the details of the ENSO cycles that they exhibit. Probably the most striking difference between the two models is in the way that atmospheric heating is computed. In the K93 model, atmospheric heating occurs in two ways: firstly, through direct thermal forcing induced by SST anomalies, which represents the effects of radiation, sensible heating and shallow atmospheric convection not parametrized in the model; secondly, through latent heating in anomalous deep penetrative convection that is induced by the warm SSTs in the western tropical Pacific where SST exceeds 28°C and is high enough for such convection to occur. In the Zebiak and Cane model, atmospheric heating occurs through surface evaporative anomalies via a linearized Clausius–Clapeyron relation, and through latent heating that occurs when the total-wind field (seasonal climatology plus the anomaly) is convergent. This latent heating occurs primarily over the east-central and south-west Pacific where seasonal variations in the Intertropical Convergence Zone (ITCZ) and South Pacific Convergence Zone are modulated by the seasonally varying convergent trade-winds. These differences in the source of latent heating in the two models lead to SVs that have dynamical centres of action in different parts of the Pacific basin. In the Kleeman

model, SV action is mainly confined to the central and western Pacific, determined by the necessary conditions (A) to (D) discussed in section 4; in the Zebiak and Cane model, SV action is primarily confined to the central and eastern Pacific (Chen *et al.* 1997; Xue *et al.* 1996), suggesting either that the ITCZ is the more important of the two climatological zones of atmospheric wind convergence in that model, or that surface evaporative-heating anomalies dominate. This may be because SST in the Zebiak and Cane model is most sensitive to changes in the ocean circulation in the eastern tropical Pacific where the main thermocline is shallow.

It is potentially dangerous to make claims, based on calculations using a model ENSO cycle, about the effect of the real ENSO cycle on perturbation growth since such conclusions are likely to be model dependent. With this in mind, we shall discuss the likely effect that the observed ENSO-signal will have on the SVs studied earlier. For this purpose, we have used the composite El Niño described by Rasmusson and Carpenter (1982) (hereafter RC82) as a source of reference, and we shall discuss its most likely influence on SV growth by drawing on our knowledge of the SV dynamics explored in MK96 and in section 4. Implicit in this analysis is the assumption that surface-driven deep penetrative convection is an important driving force for perturbations in the real atmosphere over the western tropical Pacific Ocean; based on the observations, for example, of Lau and Chan (1985), Hendon and Glick (1997) and Jones and Weare (1996), this assumption seems to be a reasonable one. It has an important bearing, not only on the ways in which the ENSO cycle may affect the growth of errors which result from deep penetrative convection in the 'atmosphere' of a realistic coupled model, but also on the way in which perturbations in the natural coupled-system could alter the whole course of a real ENSO episode. The latter issue will be considered in more detail in Part II.

In the following, we have assumed that the SST- and wind-anomalies of El Niño and La Niña episodes evolve as mirror images of each other. We know from observation that this is not necessarily the case in nature, but in the absence of a detailed analysis of La Niña like that of RC82 for El Niño, the mirror-image assumption will suffice. Throughout section 4, the importance of nonlinearity in the basic-state flow was highlighted by the conditions (A) to (D) that are necessary conditions for rapid perturbation-growth to occur. Now we use our knowledge of these conditions to speculate on the possible influence of nonlinearity in nature on the growth of perturbations governed by the same dynamics as the different classes of SVs examined in section 4. Because of nonlinearity, the influences of El Niño and La Niña on a SV will not be simple opposites: consider the effect on perturbations of basic-state nonlinearities described by (7), (10) and (11). The basic-state fields of Q, h, $\overline{w}$, w and so on in these expressions will not be the same during different phases of the basic-state ENSO cycle, so the switches described by (7), (10) and (11) will not be active at the same times or locations during different phases of the ENSO cycle.

The remainder of this section illustrates the use of our knowledge of the dynamics of rapid perturbation growth, gained from studying SVs, to increase our understanding of the factors that are likely to influence perturbation growth in the real coupled system.

(*a*) *El Niño*

Based on the findings of section 4, the likely influence of the observed El Niño cycle on each class of SV is summarized in Fig. 7. Each panel in Fig. 7 shows a schematic of the SST and wind anomalies of the composite El Niño studied by RC82. In referring to Fig. 7, we have used the nomenclature of RC82 to refer to the different phases of an El Niño episode, and the ENSO cycle is described in terms of the anomaly fields T', u, w, q and $\mathbf{U}$ in (1), (2), (8) and (9).

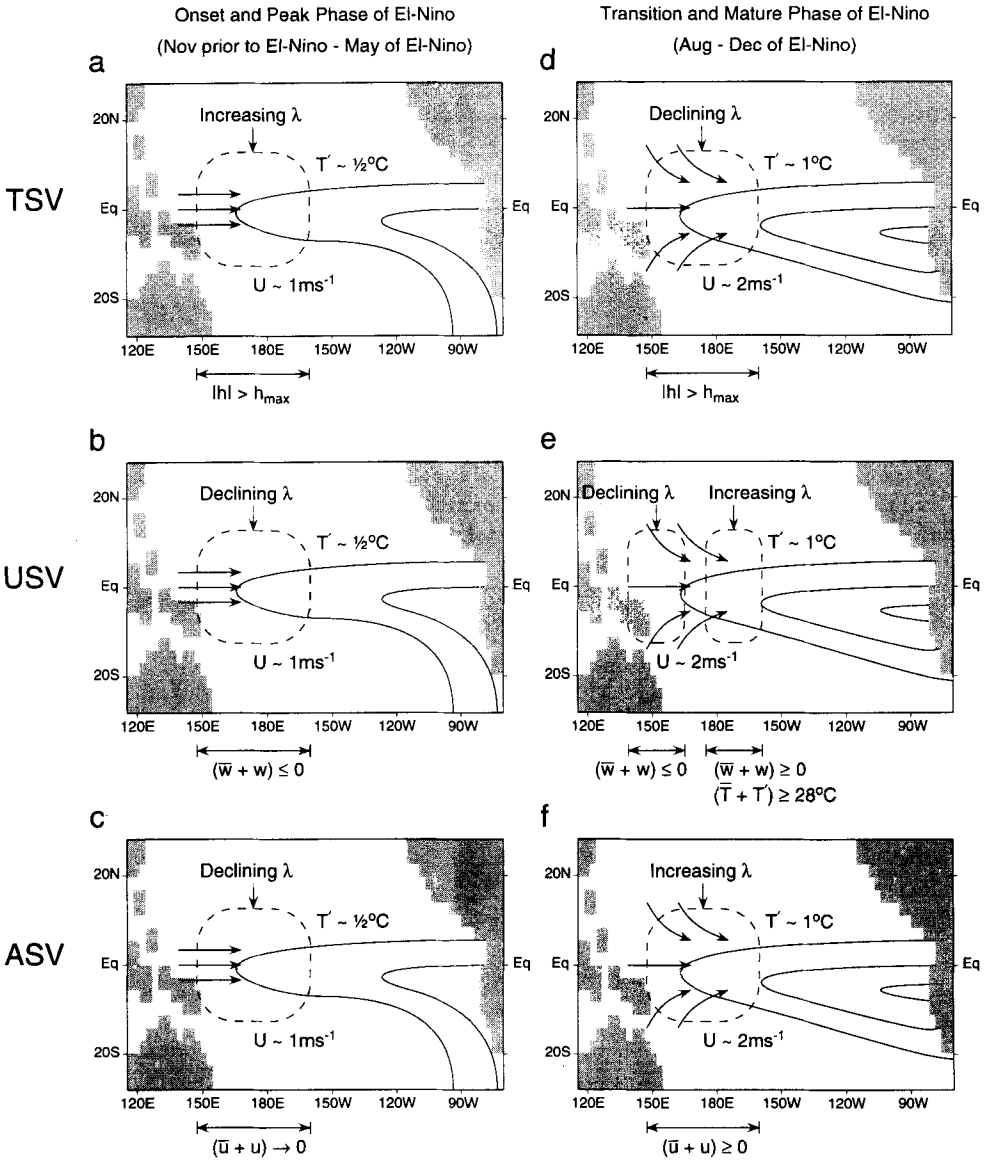

Figure 7. A schematic summarizing the influence that the observed El Niño signal is likely to have on each class of SV studied in section 4. The contours and arrows indicate the extent of positive SST-anomalies and westerly-wind anomalies respectively, and are drawn according to the composite El Niño of Rasmusson and Carpenter (1982). The regions enclosed by dashed lines indicate where the perturbation-energy growth-factor λ is likely to increase or decrease when compared to its value in the presence of the observed seasonal cycle alone (cf. Table 1). The conditions giving rise to the indicated trend in λ are shown below each panel.

During the onset and peak phases of El Niño*, the central Pacific warms by around 1/2°C, creating conditions more favourable for deep penetrative convection in the atmosphere (condition (A) of section 4). However, at the same time, the trade winds weaken or reverse in the western Pacific, producing changes in upwelling w and zonal-wind anomaly $\mathbf{U}$ of approximately 1 m s^{-1}. Initially, the warming of the central Pacific will enhance the ability of TSV to grow (Fig. 7(a)) because the thermocline nonlinearity (10) remains

* From November of the year before El Niño to May of the El Niño year.

inactive. For USV (Fig. 7(b)), the important effects of nonlinearity in the basic state are described by (11). During the onset and peak phases of El Niño, westerly wind anomalies induce downwelling anomalies, $w \leqslant 0$. In the western Pacific, $(\overline{w} + w)$ in (11) is likely to become zero or negative (since $\overline{w}$ is small there for most of the year) so that further changes in δw will not influence SST, and the ability of USV to grow will decline. These same westerly wind anomalies will promote anomalous eastward surface-currents, $u \geqslant 0$. As a result, since $\overline{u} < 0$, $(\overline{u} + u)$ is likely to decrease, which will lead to a decline in the ability of ASV to grow in the western Pacific (Fig. 7(c)) through the action of $(\overline{u} + u)\partial\delta T'/\partial x$ in (9).

During the transition and mature phases of El Niño*, the central Pacific Ocean warms further, creating conditions even more favourable for deep penetrative convection in the atmosphere. At this time, the thermocline is deep and the thermocline nonlinearity described by (10) is invoked, so growth of TSV is inhibited (Fig. 7(d)); see MK96. Similar results have been reported by Chen *et al.* (1997). As the westerly wind anomalies of El Niño strengthen and move eastward (**U** can be up to 3 m s^{-1}), downwelling in the western Pacific ($\overline{w} + w < 0$ in (11)) inhibits growth of USV (Fig. 7(e)). However in the central Pacific, upwelling is still likely and higher than normal SSTs there ($T' \approx 1°C$) can enhance the growth of USV because conditions there are more favourable for deep penetrative convection. From August to November, $\overline{u} > 0$ in the western Pacific (cf. Fig. 3(d)), so the westerly wind anomalies of El Niño can enhance the seasonal cycle of $\overline{u}$, creating conditions more favourable for the growth of ASV (Fig. 7(f)) over the western and central Pacific where $(\overline{u} + u) > 0$ and SST > 28°C.

We can view the behaviour of the different classes of SVs discussed above as an indication of the potential ability of perturbations to grow via surface-forced deep penetrative convection in the atmosphere that is triggered by the influence of different thermodynamic mechanisms operating on SST. Figure 7 therefore gives an indication of the influence an observed El Niño episode is likely to have on the growth of perturbations resulting from each thermodynamic process. The overall effect of an El Niño on perturbation growth will depend on the relative importance of the different thermodynamics processes that control SST.

(*b*) *La Niña*

As mentioned earlier, we will assume, for the sake of argument, that during La Niña, SST and wind anomalies evolve as the negative image of the composite El Niño described by RC82. The likely influence of La Niña on each class of SV is summarized in Fig. 8. Each panel of Fig. 8 shows a schematic of the SST and wind anomalies that might accompany a typical La Niña event. As noted above, the influence that nonlinearities in the basic-state flow have on perturbation development (cf. (7), (10) and (11)) ensures that the influence of a La Niña event is not simply the opposite of that of an El Niño event.

During the onset and peak phases of La Niña†, the central Pacific begins to cool by about 1/2°C and the western Pacific warm-pool begins to recede westwards. In the central Pacific, this creates conditions unfavourable for deep penetrative convection and the inherent ability of all SVs to grow there declines (Fig. 8(a,b,c)). Associated with the negative SST-anomalies are easterly-wind anomalies $\mathbf{U} \sim 1$ m s^{-1}. These will promote upwelling in the western Pacific ($\overline{w} + w \geqslant 0$), so, according to (11), the ability of USV to grow may increase there (Fig. 8(b)). Similarly, the easterly-wind anomalies will enhance

* Between August and December of the El Niño year.

† Between November of the year before a La Niña event and May of the La Niña year.

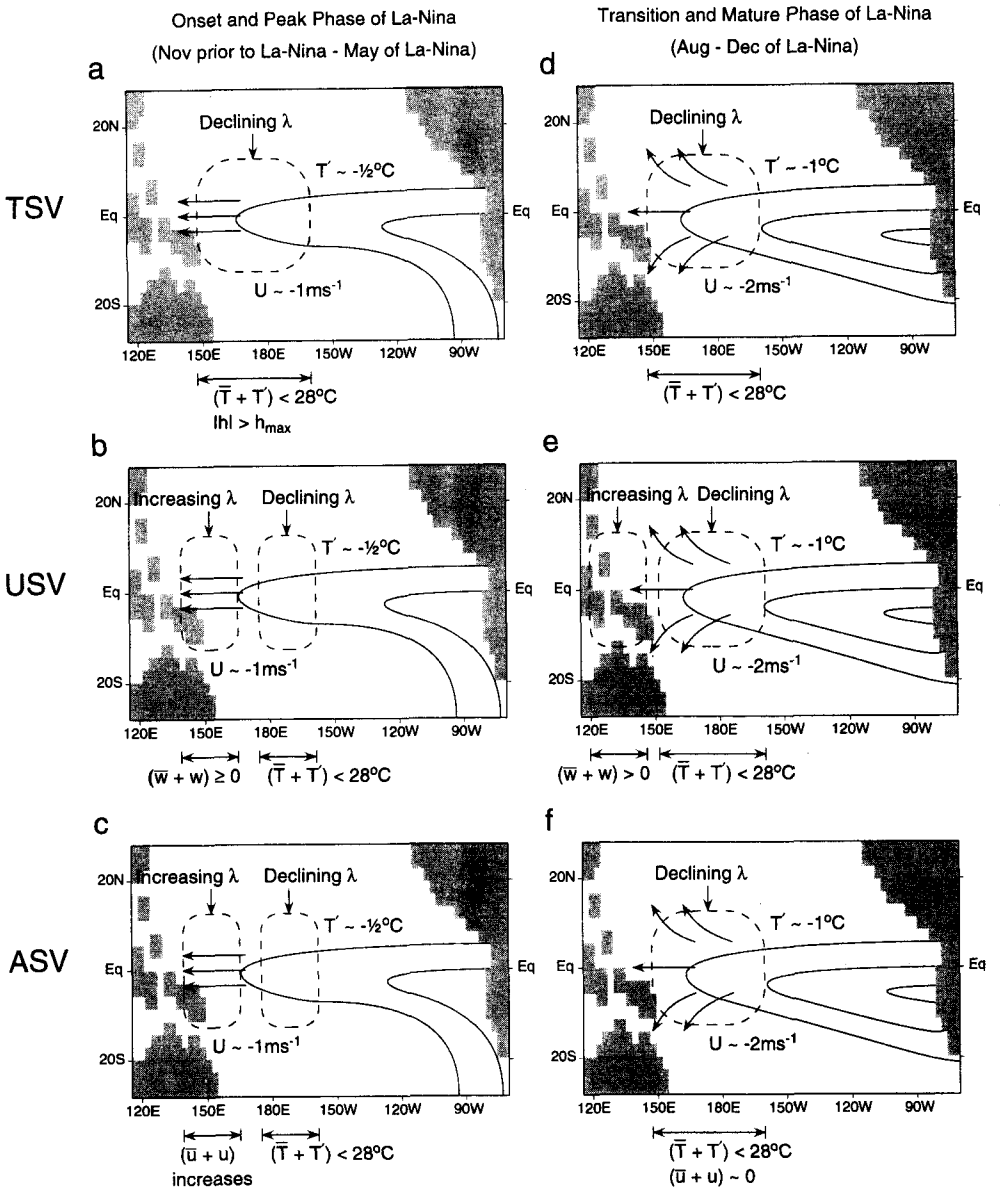

Figure 8. As Fig. 7, but for the case of a La Niña event. The La Niña is assumed to develop as the negative image of the composite El Niño of Rasmussen and Carpenter (1982). Contours and arrows are a schematic representation of negative SST-anomalies and easterly-wind anomalies respectively according to Rasmussen and Carpenter (1982).

the easterly trade-winds of the seasonal cycle, creating conditions in the far western Pacific that may be more favourable for the growth of ASV via $(\bar{u} + u)\partial\overline{T}/\partial x$ in (9) (Fig. 8(c)).

By the time of the transition and mature phase*, the central Pacific is at least 1°C colder than normal so conditions will be very unfavourable for deep penetrative convection here. All SVs are likely to undergo a decline in their ability to grow in the central Pacific (Fig. 8(d,e,f)). In response to the strong easterly-wind anomalies of a La Niña in the far

* Between August and December of the La Niña year.

western Pacific, upwelling may intensify, so, according to (11), the ability of USV to grow over warm water in this region may increase (Fig. 8(e)). During the period from August to November, $\overline{u} > 0$, in which case the easterly-wind anomalies of La Niña can significantly weaken the total current $(\overline{u} + u)$. This may lead to a reduction in the ability of ASV to grow (Fig. 8(f)) even if the surface waters are still warm enough for deep penetrative convection to occur.

6. Discussion

By computing the singular vectors of the system, we have examined the mechanisms that can give rise to rapid perturbation-growth in a coupled ocean–atmosphere model of the tropics. The singular vectors are the most rapidly growing perturbations that can exist in the system before they are affected by nonlinearity. This work is clearly relevant to the growth of errors and uncertainties in coupled models used to predict El Niño, and to the way in which such errors influence the forecast skill of a model. The singular vectors reveal much information about the likely properties and behaviour of errors in coupled models. With this in mind, references in the ensuing discussions to 'perturbations' will be taken to be synonymous with references to errors. However, the results presented here are also relevant to the development of perturbations in nature and to ways in which different environmental factors may influence them.

The influence of the upper-ocean thermodynamics (which controls SST) on the SVs was investigated by considering (a) vertical movements of the main ocean thermocline in the presence of mean equatorial upwelling, (b) changes in the rate of equatorial upwelling, and (c) zonal advection of heat by ocean currents. As a result of our investigations, we can comment as follows on the growth of errors and perturbations in coupled models.

(i) The SV spectrum is always dominated by its fastest-growing member.

(ii) Each thermodynamic process operating in the upper ocean gives rise to a different class of SVs although the structure of the dominant SV wind-field in each class is relatively insensitive to different combinations of thermodynamic processes.

(iii) For each class of SV considered, error growth in the atmosphere is dominated by latent-heat release resulting from convergence of the mean moisture field caused by wind errors. As discussed by MK96, error growth due to atmospheric-moisture-convergence heating could occur in other models, such as that of Zebiak and Cane (1987), and in coupled GCMs, so we believe that our results are widely applicable to the ENSO prediction problem.

(iv) Error growth in the atmosphere is initiated by SST perturbations that develop in response to perturbations in the ocean circulation. We have found that for rapid error-growth to occur in the atmosphere, two conditions must be satisfied simultaneously:

- deep penetrative convection must be possible in the atmosphere and can only occur when SST $\geqslant 28°C$;
- SST perturbations must be sensitive to perturbations in the ocean circulation.

Based on dynamical arguments, these conditions can be satisfied simultaneously only in the western and central tropical Pacific.

(v) The preferred regions of error growth are independent of the upper-ocean thermodynamics, with growth occuring primarily in the western and central tropical Pacific. Other areas of growth also appear from time to time, depending upon the phase of the seasonal cycle and the timescale over which errors can grow. During boreal summer, a small region north of the equator in the eastern Pacific Ocean, off the coast of Central America, can

host rapid error-growth. Rapid error-growth on timescales of about one or two months can also occur over the Philippines, particularly during the onset of the Asian monsoons. This suggests that the potential for error growth in coupled GCMs could be very large in the far western Pacific, since this is a region of intense convective activity in such models and initial-condition errors here can be rapidly amplified.

(vi) The growth of TSV depends critically on the presence of an initial-thermocline perturbation δh. As shown by MK96, rapid error-growth is possible when the coupled model is initialized with only the δh component of TSV. In the case of USV and ASV, δh has no influence on SST since $\eta = 0$ in (10) and it is found that the initial SST perturbations of these SVs are critical for their growth. In these cases, the large-scale initial SST creates wind perturbations that induce perturbations in upwelling and zonal velocity that lead to SV growth. In the case of TAUSV, all thermodynamic processes influence $\delta T'$. If only the initial δh of a TAUSV is used to initialize the model, growth of the subsequent perturbation is generally slower than if $\delta T'$ of TAUSV is used. This is because, in response to the initial δh, only one thermodynamic process is initially acting on SST, so the system must develop a $\delta T'$ and wind perturbation in order to achieve perturbation growth through changes in upwelling and zonal advection as well. On the other hand, in response to an initial $\delta T'$, the perturbation can grow via the immediate action of two thermodynamic processes resulting from changes in upwelling and zonal advection. As δh develops, it can influence perturbation growth later on.

Thermocline perturbations δh can initially develop in the ocean away from SST perturbations $\delta T'$. On the other hand, long lived $\delta T'$ (persisting for a period of some weeks) are less likely to begin to develop away from δh, since $\delta T'$ would be damped by negative-feedback processes. In the tropics, it is likely that $\delta T'$ largely arise from perturbations to the ocean circulation. Therefore, we expect that δh will be more effective at initiating error growth than will equatorial upwelling and horizontal advection, because errors can only develop via these latter two processes in response to $\delta T'$, and $\delta T'$ is unlikely to develop until δh does so. These ideas are consistent with the experience of operational ENSO-forecasting which indicates that the forecast skill of such systems tends to decrease most rapidly during boreal spring. Our experiments with TSVs show that this is consistent with rapid error growth at this time resulting from errors in the thermocline depth. The TSVs grow most rapidly during spring, whereas SVs resulting from other combinations of thermodynamic processes grow fastest later in the year.

Thermocline perturbations will develop in the ocean due to the presence of transient equatorial ocean-waves. In a forecasting environment, there are a number of ways that such waves can appear in a coupled model. These include: the generation of waves by errors and uncertainties in the initial conditions in the model; the excitation of waves through geostrophic adjustment of initial conditions which are not in exact dynamic balance (a problem commonly referred to as 'initialization shock' in numerical weather-prediction), and the appearance of waves in response to stochastic noise-forcing inherent in the system.

We expect that error growth in coupled models will develop in response to thermocline movements induced by erroneous transient equatorial ocean-waves, which in turn will generate SST errors. In response to the SST errors, errors in the atmospheric circulation will grow, and as wind errors and SST errors develop further, equatorial upwelling and horizontal advection can play a role in amplifying the errors if conditions are favourable. If the erroneous transient equatorial ocean-wave activity in a coupled model is reduced in some way, then error-growth activity should decrease, resulting in an increase in forecast skill. The recent experiments of Chen *et al.* (1995), using the model of Zebiak and Cane (1987), certainly support this idea.

(vii) The final configuration of the error-growth wind-patterns associated with the coupled-model SVs is relatively insensitive to the upper-ocean thermodynamics and the phase of the seasonal cycle. This stems from the fact that the moisture-flux-convergence term $\delta E_{\mathrm{mc}} = -B\delta\Phi\overline{q}\nabla\cdot\delta\mathbf{U}/4\epsilon c^2$ (arising from perturbation deep penetrative convection in the atmosphere) accounts for most of the growth in perturbation energy in the coupled model. For δE_{mc} to grow, the SVs must produce a wind field $\delta\mathbf{U}$ which evolves with time and is favourably configured in the sense that it has non-zero divergence ($\nabla\cdot\delta\mathbf{U}\neq 0$) in regions where the background specific humidity $\overline{q}$ is large. For a given time series of seasonally varying $\overline{q}$, there is a pattern of wind-field divergence $\nabla\cdot\delta\mathbf{U}$ that is optimal in the sense that it leads to rapid growth of δE_{mc}. To achieve rapid perturbation energy-growth, thermodynamic processes operating in the upper ocean will combine to produce a SV SST pattern that will generate the optimal wind-field divergence. All this suggests that, in the tropics, the coupled system has a preferred response to errors—a response that will readily manifest itself if conditions are favourable. These findings have important ramifications for the way in which the real ocean–atmosphere system will respond to the ubiquitous high-frequency events which occur in the atmosphere such as synoptic weather variations, diurnal variations in convective activity, and 30–60 day waves. Our results also reveal that the rate of growth of such perturbations will be sensitive to a number of environmental factors. Clearly, the turn of events in nature could be influenced considerably by rapidly growing perturbations if they attain large amplitude. This is perhaps one explanation for the differences between observed ENSO events: no two events of the same kind evolve in the same way. We will discuss these issues further in Part II.

(viii) Based upon our knowledge of the perturbation-growth mechanisms, and the criteria that are necessary for rapid perturbation-growth to occur, we have postulated the influence that the observed ENSO cycle is likely to have on the growth of perturbations that resemble SVs. Taking into account the relative importance of different upper-ocean thermodynamic processes on SST, we can infer how the ENSO cycle may influence perturbation growth under different scenarios. For instance, if all thermodynamic processes are equally important, we might expect SST thermocline-depth perturbations during the onset of an El Niño to enhance perturbation growth in the western and central Pacific. During this time, equatorial upwelling and zonal advection are likely to be relatively ineffective at promoting SST perturbation-growth. As an El Niño matures, the rapidly deepening thermocline will render thermocline perturbations ineffective in promoting further SST perturbation-growth; equatorial upwelling and zonal advection in the central Pacific, on the other hand, are likely to become more effective in this regard. So, if, during the course of an El Niño episode, all thermodynamic processes are equally important in controlling SST perturbations we might expect an overall decline in the ability of perturbations to grow in the western tropical Pacific, accompanied by an increase in their ability to grow in the central tropical Pacific. We might also expect that, during the onset and mature development of a La Niña, the large-scale cooling that occurs in the western and central Pacific will make the thermodynamic processes which influence SST relatively ineffective at promoting SST-perturbation growth. In the far west Pacific however, rapid SST-perturbation growth might still be possible as a result of equatorial upwelling and zonal advection near the Philippines. These ideas lend further weight to the conclusion of MK96 that the onset of an El Niño is likely to be less predictable than the onset of a La Niña.

Singular-vector calculations have also been performed by Blumenthal (1991) and Xue *et al.* (1994, 1997) using the coupled model of Zebiak and Cane (1987), and by Chen *et al.* (1997) using the Battisti (1988) version of the Zebiak and Cane model. While the structures of the SVs computed in our study show some similarity with those of these other studies,

there are also differences. These can be attributed to differences between the models used. However, some aspects of the SV behaviour computed here, and in MK96, are similar to the behaviour found in other studies. In particular, the SV spectrum is dominated by its fastest-growing member. The structure of this member is relatively insensitive to the time of year, and it can act as a precursor for ENSO events in each coupled model. No discussion of the energetics of SV growth is given by the workers cited, so we cannot compare this aspect of our results with theirs. Using the observed record of SST in the Indian and Pacific Oceans, Penland and Sardeshmukh (1995) have computed the SST structure of the dominant SV of the perturbation-SST norm. The large-scale SST structure of their SV in the Pacific bears some similarity to the structure of some of the SVs computed here and those of the other cited workers. However, there are many small-scale features present in the SV of Penland and Sardeshmukh which may or may not be real, and which cannot be captured with models like that used here. Verification of the SV patterns derived from observations will have to await similar calculations performed with realistic coupled GCMs.

ACKNOWLEDGEMENTS

We are indebted to Professor Dan Sorensen, Richard Lehoucq and Phuong Vu at Rice University for making their Lanczos and Arnoldi algorithm software available to us. Without these subroutines, many of the calculations reported in this paper would not have been possible. Andrew Moore also wishes to acknowledge the support of the Nova Southeastern University Oceanographic Center.

REFERENCES

Barnett, T. P., Bengtsson, L., Arpe, K., Flügel, M., Graham, N., Latif, M., Ritchie, J., Roeckner, E., Schlese, U., Schulzwieda, U. and Tyree, M. 1994 Forecasting global ENSO-related climate anomalies. *Tellus*, **46A**, 381–397

Barnston, A. G., van den Dool, H. M., Zebiak, S. E., Barnett, T. P., Ji, M., Rodenhuis, D. R., Cane, M. A., Leetmaa, A., Graham, N. E., Ropelewski, C. R., Kousky, V. E., O'Lenic, E. O. and Livezey, R. E. 1994 Long-lead seasonal forecasts—Where do we stand? *Bull. Amer. Meteorol. Soc.*, **75**, 2097–2114

Battisti, D. S. 1988 Dynamics and thermodynamics of a warming event in a coupled tropical atmosphere–ocean model. *J. Atmos. Sci.*, **45**, 2889–2919

Battisti, D. S. and Hirst, A. C. 1989 Interannual variability in a tropical atmosphere–ocean model: Influence of the basic state, ocean geometry and nonlinearity. *J. Atmos. Sci.*, **46**, 1687–1712

Blumenthal, M. B. 1991 Predictability of a coupled ocean–atmosphere model. *J. Climate*, **4**, 766–784

Buizza, R. and Palmer, T.N. 1995 The singular-vector structure of the atmospheric global circulation. *J. Atmos. Sci.*, **52**, 1434–1456

Buizza, R., Tribbia, J., Molteni, F. and Palmer, T.N. 1993 Computation of optimal unstable structures for a numerical weather prediction model. *Tellus*, **45A**, 388–407

Cane, M. A. and Sarachik, E. S. 1981 The response of a linear baroclinic equatorial ocean to periodic forcing. *J. Mar. Res.*, **35**, 395–432

Chen, D., Zebiak, S. E., Busalacchi, A. J. and Cane, M.A. 1995 An improved procedure for El Niño forecasting. *Science*, **269**, 1699–1702

Chen, Y.-Q., Battisti, D. S., Palmer, T. N., Barsugli, J. and Sarachik, E. S. 1997 A study of the predictability of tropical Pacific SST in a coupled atmosphere/ocean model using singular vector analysis: The role of the annual cycle and the ENSO cycle. *Mon. Weather Rev.*, In press

Davey, M. K. and Gill, A. E. 1987 Experiments on tropical circulation with a moist model. *Q. J. R. Meteorol. Soc.*, **113,** 1237–1270

Farrell, B. F. 1982 The initial growth of disturbances in baroclinic flow. *J. Atmos. Sci.*, **39,** 1663–1686

1985 Transient growth of damped baroclinic waves. *J. Atmos. Sci.*, **42,** 2718–2727

1988 Optimal excitation of neutral Rossby waves. *J. Atmos. Sci.*, **45,** 163–172

1990 Small error dynamics and the predictability of flows. *J. Atmos. Sci.*, **47,** 2409–2416

Farrell, B. F. and Moore, A. M. 1992 An adjoint method for obtaining the most rapidly growing perturbation to oceanic flows. *J. Phys. Oceanogr.*, **22,** 338–349

Gill, A. E. 1980 Some simple solutions for heat-induced torpical circulation. *Q. J. R. Meteorol. Soc.*, **106,** 447–462

1982 *Atmosphere–ocean dynamics*, Academic Press

1985 Elements of coupled ocean–atmosphere models for the tropics. *Coupled Ocean–Atmosphere Models*, Elsevier, 303–327

Goswami, B. N. and Shukla, J. 1991 Predictability of a coupled ocean–atmosphere model. *J. Climate*, **4,** 3–22

Hendon, H. H. and Glick, J. 1997 Intraseasonal air–sea interaction in the tropical Indian and Pacific Oceans. *J. Climate*. In press

Hirst, A. C. 1986 Unstable and damped equatorial modes in simple coupled ocean–atmosphere models. *J. Atmos. Sci.*, **43,** 606–630

Jones, C. and Weare, B. C. 1996 The role of low-level moisture convergence and ocean latent-heat fluxes in the Madden and Julian Oscillation: An observational analysis using ISCCP data and ECMWF analyses. *J. Climate*, **9,** 3086–3104

Kleeman, R. 1989 A modelling study of the effect of the Andean mountains on the summertime circulation of tropical South America. *J. Atmos. Sci.*, **46,** 3344–3362

1991 A simple model of the atmospheric response to ENSO sea surface temperature anomalies. *J. Atmos. Sci.*, **48,** 3–18

1993 On the dependence of hindcast skill on ocean thermodynamics in a coupled ocean–atmosphere model. *J. Climate*, **6,** 2012–2033

Kleeman, R. and Moore, A. M. 1997 A theory for the limitations of ENSO predictability due to stochastic atmospheric transients. *J. Atmos. Sci.*, In press

Kleeman, R., Latif, M. and Flügel, M. 1992 A hybrid tropical atmosphere ocean model: Sensitivities and hindcast skill. *Max Planck Institut für Meteorologie Report* **76**

Kleeman, R., Moore, A. M. and Smith, N. R. 1995 Assimilation of sub-surface thermal data into an intermediate tropical coupled ocean–atmosphere model. *Mon. Weather Rev.*, **123,** 3103–3113

Latif, M. and Graham, N. E. 1991 How much predictive skill is contained in the thermal structure of an ocean? *TOGA Notes*, **2,** 6–8

Latif, M., Sterl, A., Maier-Reimer, E. and Junge, M. M. 1993 Climate variability in a coupled GCM. Part I: The tropical Pacific. *J. Climate*, **6,** 5–21

Latif, M., Barnett, T. P., Cane, M. A., Fügel, M., Graham, N. E., von Storch, H., Xu, J.-S. and Zebiak, S. E. 1994 A review of ENSO prediction studies. *Climate Dynamics*, **9,** 167–179

Lau, K.-M. and Chan, P. H. 1985 Aspects of the 40–50 day oscillation during the northern winter as inferred from outgoing long-wave radiation. *Mon. Weather Rev.*, **113,** 1889–1909

Legler, D. M. and O'Brien, J. J. 1984 *The atlas of tropical Pacific wind-stress climatology 1971-1980.* Florida State University

Lorenz, E. N. 1965 A study of the predictability of a 28-variable atmospheric model. *Tellus*, **17,** 321–333

Molteni, F. and Palmer, T.N. 1993 Predictability and finite-time instability of the northern winter circulation. *Q. J. R. Meteorol. Soc.*, **119,** 269–298

Moore, A. M. and Farrell, B. F. 1993 Rapid perturbation growth on spatially and temporally varying oceanic flows determined using an adjoint method: Application to the Gulf Stream. *J. Phys. Oceanogr.* **23,** 1682–1702

Moore, A. M. and Farrell, B. F. 1994 'Using adjoint models for stability and predictability analysis'. Pp. 217–239 in *Data assimilation: a new tool for modelling of the ocean in a global change perspective.* NATO ASI Series, **19,** P. P. Brasseur and J. C. J. Nihoul, Eds., Springer-Verlag

Moore, A. M. and Kleeman, R. 1996 The dynamics of error growth and predictability in a coupled model of ENSO. *Q. J. R. Meteorol. Soc.*, **122,** 1405–1446

1997 The singular vectors of a coupled ocean–atmosphere model of ENSO. II: sensitivity studies and dynamical interpretation. *Q. J. R. Meteorol. Soc.*, **123,** 983–1006

Morse, D. M. and Feshbach, H. 1953 *Methods of theoretical physics: Vol. I,* McGraw Hill Book Company Inc.

Mureau, R., Molteni, F., and Palmer, T. N. 1993 Ensemble prediction using dynamically-conditioned perturbations. *Q. J. R. Meteorol. Soc.*, **119,** 299–323

Neelin, J. D. 1990 A hybrid coupled general circulation model for El Niño studies. *J. Atmos. Sci.*, **47,** 674–693

1991 The slow sea surface temperature mode and the fast-wave limit: Analytic theory for tropical interannual oscillations and experiments in a hybrid coupled model. *J. Atmos. Sci.*, **48,** 584–606

Neelin, J. D., Latif, M., Allaart, M. A. F., Cane, M. A., Cubasch, U., Gates, W. L., Gent, P. R., Ghil, M., Gordon, C., Lau, N.-C., Mechoso, G. A., Meehl, G. A., Oberhuber, J. M., Philander, S. G. H., Schopf, P. S., Sperber, K. R., Sterl, A., Tokioka, T., Tribbia, J. and Zebiak, S. E. 1992 Tropical air–sea interaction in general circulation models. *Climate Dynamics*, **7,** 73–104

Palmer, T. N. 1993 Extended-range atmospheric prediction and the Lorenz model. *Bull. Amer. Meteorol. Soc.*, **74,** 49–65

Palmer, T. N. and Anderson, D. L. T. 1994 The prospects for seasonal forecasting—A review paper. *Q. J. R. Meteorol. Soc.*, **120,** 755–793

Palmer, T. N., Buizza, R., Molteni, F., Chen Y.-Q. and Corti, S. 1994 Singular vectors and predictability of weather and climate. *Phil. Trans. R. Soc. Lond. A*, **348,** 459–475

Penland, C. and Sardeshmukh, P. D. 1995 The optimal growth of tropical sea surface temperature anomalies. *J. Climate*, **8,** 1999–2024

Phlips, P. J. 1987 A simple model of the wind-driven tropical ocean. *J. Phys. Oceanogr.*, **17,** 2003–2015

Rasmusson, E. M. and Carpenter, T. H. 1982 Variations in tropical sea surface temperature and surface winds associated with the Southern Oscillation/El Niño. *Mon. Weather Rev.*, **110,** 354–384

Rosati, A., Miyakoda, K. and Gudgel, R. 1997 The impact of ocean initial conditions on ENSO forecasting with a coupled model. *Mon. Weather Rev.* In press

Xue, Y., Cane, M. A., Zebiak, S. E. and Blumenthal, M. B. 1994 On the prediction of ENSO: A study with a low order Markov model. *Tellus*, **46A,** 512–528

Xue, Y., Cane, M. A. and Zebiak, S. E. 1997 Predictability of a coupled model of ENSO using singular vector analysis. Part I: Optimal growth in seasonal background and ENSO cycles. *Mon. Weather Rev.* In press

Zebiak, S. E. and Cane, M. A. 1987 A model of El Niño Southern Oscillation. *Mon. Weather Rev.*, **115,** 2262–2278